IS-T--1815

Microstructure-strength Relationships of Heavily Deformed Magnesium-lithium Composites Containing Steel Fibers

by

Jensen, Jeff

PHD Thesis submitted to Iowa State University

Ames Laboratory, U.S. DOE

Iowa State University

Ames, Iowa 50011

Date Transmitted: October 8, 1997

PREPARED FOR THE U.S. DEPARTMENT OF ENERGY

UNDER CONTRACT NO. W-7405-Eng-82.

DISCLAIMER

AVAILABILITY:

To DOE and DOE contractors: Office of Scientific and Technical Information
P.O. Box 62
Oak Ridge, TN 37831

prices available from: (615) 576-8401
FTS: 626-8401

To the public: National Technical Information Service
U.S. Department of Commerce
5285 Port Royal Road
Springfield, VA 22161

DISCLAIMER

Portions of this document may be illegible electronic image products. Images are produced from the best available original document.

TABLE OF CONTENTS

Preprint — Removed for separate processing

Preprint — Removed for separate processing

Preprint — Removed for Separate Processing

ABSTRACT

The successful development of deformation-processed metal-metal composites (DMMC) offers the potential for ductile, high-strength structural materials with high-temperature stability. An infiltration casting process, developed as an alternative method to combine matrix and fiber materials with dissimilar melting temperatures, was used to permeate steel wool preforms with molten magnesium-lithium (Mg-Li) alloys. The selected matrix alloys were hexagonal close packed (HCP) Mg-4wt%Li or body centered cubic (BCC) Mg-12wt%Li; the low carbon steel wool fibers were predominantly BCC ferrite. These cast HCP/BCC and BCC/BCC composites were deformed by rolling or by extrusion and swaging. Mechanical properties, microstructure, and texture development of the composites were characterized at various levels of deformation. The HCP/BCC composites had limited formability at temperatures up to 400°C while the BCC/BCC composites had excellent formability during sheet rolling at room temperature but limited formability during swaging at room temperature. The tensile strengths of these HCP/BCC and BCC/BCC composite materials increased moderately with deformation, though less than predicted from rule of mixtures (ROM) calculations. The microstructure was characterized to correlate the filament size to the deformation strain and mechanical properties of the composite material. Stereological measurements of the filament size were used to adjust ROM calculations to reflect the actual deformation strain in the fibers. However, the experimental strengths of these composite materials were still less than ROM predictions, possibly due to the presence of considerably large fibers. Of the many models used to describe the strengthening observed in DMMC materials, the Hall-Petch relationship adequately described the experimental data. Texture development was also characterized to explain the deformation characteristics of the composite materials. Pole figures for the matrix and fiber phases at various levels of deformation were obtained using X-ray diffraction and orientation imaging

microscopy (OIM). Texture analysis results were compared to the development of specific microstructures during deformation and to the limited deformation characteristics observed for some of the composite materials. OIM had not been used previously for the texture analysis of DMMC materials and the advantages of this technique were compared to conventional X-ray methods.

CHAPTER 1: GENERAL INTRODUCTION

World-wide development work on light metal alloys has fallen into a somewhat unimaginative pattern of pursuing one of two strategies: 1) fine-tuning alloy compositions to tweak small performance improvements from solid solution hardening and precipitation hardening mechanisms, or 2) developing various means to disperse ceramic particles/fibers in a metal matrix. While both strategies have had considerable success, light metal alloys are only now being introduced into applications where heavier steel alloys have traditionally been used, e.g. automobile seat frames. This is due to two basic reasons. Firstly, the performance improvements seen are not great enough to overtake the properties of steel in many cases, particularly for elevated temperature applications. Secondly, where the properties of composite alloys do rival those of steel, the high cost of producing the composite material often precludes its widespread usage. The general adoption of light-weight alloys awaits the development of new methods of processing and strengthening these materials that will allow them to compete with steel on both a cost and performance basis.

Given the above considerations the overall goal of this study was to investigate the possibility of developing a low cost method for producing a high-strength, light-weight alloy. A review of the current literature suggested that it might be possible to develop a suitable Mg based alloy using a combination of proper alloy selection and thermo-mechanical processing to produce a composite material that exceeds the mechanical properties of currently used alloys. Thus, the objectives of this project were to: 1) develop a low-cost alternative processing route for the production of ductile, high-strength Mg-based composite materials, 2) study the microstructure-strength relationships of these materials, and 3) determine the effects of texture development on the processing and properties of these composite materials. The fulfillment of these objectives is recorded in the pages of this dissertation. A brief rationale for the means by which the author sought to meet these objectives is given below.

There are four mechanisms which affect the strength of materials: 1) solid solution hardening, 2) precipitation hardening, 3) work hardening, and 4) microstructure hardening [1]. Of these strengthening mechanisms, only the first two are used in commercially produced structural Mg alloys. The strength of deformation-processed metal-metal composites (DMMC) is due to microstructure hardening as the sizes of the matrix and fiber phases are significantly reduced during deformation processing. The successful development of Mg-based DMMC materials would provide a third method for producing low-cost, structural Mg alloys. Thus, this method was chosen as the means by which the material would be strengthened.

Composites of elements which can be co-melted (e.g. Cu-Nb and Ti-Y) can often be prepared by conventional casting methods. Composites of elements with disparate melting temperatures (e.g. Mg-Fe or Mg-Ti) are typically prepared by powder processing methods, which can be labor intensive and costly to produce. In addition, while it is usually beneficial to begin with large billets of the DMMC material so the composite can be deformed to very high strains, the production of large billets by powder processing is limited by the pressure gradients inherent in the compaction process and can result in non-uniform densities in the billet. It was desirable that a low-cost alternative processing method for combining two elements with dissimilar melting points be found for the Mg composites in this study. The method must also be one that would produce large billets more easily and economically than is possible through conventional powder metallurgy techniques. Therefore, a new, inexpensive method for producing large composite Mg castings was developed for this study.

There remains much uncertainty concerning the exact reason for the high strengths noted in some DMMC materials. Several models have been developed to describe these exceptionally high strengths and are reviewed in [33]. It is apparent from these studies that a clear understanding of the strengthening present in these materials relies on a detailed knowledge of the microstructure and crystallographic texture development which result from processing. Thus, the microstructure, mechanical properties, and texture development of the

composites selected for this study were characterized with the hope that the results would shed additional light on the various strengthening models. The microstructure-strength relationships were correlated to the deformation processing of these DMMC materials and some of the more subtle aspects of the strengthening models were investigated during the course of this research.

The studies summarized in the following literature review suggest that deformation processing offers the potential to produce structurally useful nano-scale composites of HCP and/or BCC metals at reasonable cost. However, the tendency of these materials to texture into plane-straining configurations must be factored into the design of deformation processing procedures to optimize materials properties. This study provides additional information to help guide such design decisions and to provide valuable insight into the deformation characteristics of combinations of HCP and BCC phases not previously studied.

Literature Review

Deformation processing offers the potential to produce structural composites with nanoscale filaments at reasonable costs. DMMC Cu-X alloys, where Cu is a face-centered cubic (FCC) matrix and X is a body-centered cubic (BCC) metal immiscible in Cu, have highly desirable mechanical and electrical properties [2-10]. More recent studies of Ti-20Y [11-14] and Mg-20Fe, Mg-20Nb, Mg-20Ti, and Mg-8Li/5Ti [15-16] have demonstrated the potential for hexagonal close packed (HCP) phases to benefit similarly from deformation processing and have shown that texture development in the matrix and fiber phases has a significant influence on the processing and properties of the composite material.

Cu-X Composites

During the past several years, Cu-based DMMC materials have been developed with extraordinary mechanical and electrical properties [2-10]. These alloys, comprised of Cu (FCC) with 10 to 30 vol% of Nb, Ta, Cr, V, or Fe, are heavily deformed to produce a

nanometer-scale filaments of the secondary phase embedded in the Cu matrix. The Cu-20Nb system is the most thoroughly studied of these alloys and has ultimate tensile strengths (UTS) in excess of 2200 MPa after deformation to a true strain of $\eta = 12$ [6], where $\eta = \ln(A_0/A)$ and A_0 and A are the initial and final cross-sectional areas, respectively. For sheet materials, an effective deformation strain used for comparison to true deformation in rod materials is calculated as $\eta_e = (2/\sqrt{3})\eta$ [17], assuming negligible lateral spread, which corresponds to $\eta_e = (2/\sqrt{3})\ln(t_0/t)$, where t_0 and t are the initial and final thicknesses of the sheet, respectively.

The Cu-X alloys are characterized by remarkable ductility, which allows cast or powder-processed starting billets to be drawn to strains as high as $\eta = 13.4$ (99.99985% reduction in area) before breaking [9]. Such deformations represent more than an 800-fold reduction in diameter and are accompanied by a corresponding reduction in the size and spacing of the second phase. Thus, an as-cast billet of Cu-20Nb, displaying Nb dendrites with an average thickness of 5 μm, may be deformation processed at room temperature into a composite wire containing Nb filaments with an average thickness of 7 nm [10]. Such composites formed *in-situ* have tensile strengths substantially higher than those of any other Cu alloys and higher than the strengths predicted from rule-of-mixtures (ROM) calculations [18]. Figure 1 shows the UTS data for Cu, Nb, and Cu-20Nb, as well as the ROM strength predictions for Cu-20Nb through $\eta = 12$. It is evident that the Cu-20Nb wire is much stronger than ROM predictions for such a composite. Debate continues on the mechanism(s) which account for the high strengths of the Cu-X alloys, but discussion centers on the role of the nanoscale filamentary structure in impeding the generation and propagation of dislocations in both the matrix and fiber phases [19-23].

Figure 2 shows a representation of the filament morphology typically seen in transverse sections of heavily deformed DMMC rod and sheet materials. Deformation often produces ribbon-shaped filaments that remain parallel to the rolling plane in sheet materials or that become convoluted about the deformation axis in rod materials. These filaments have very

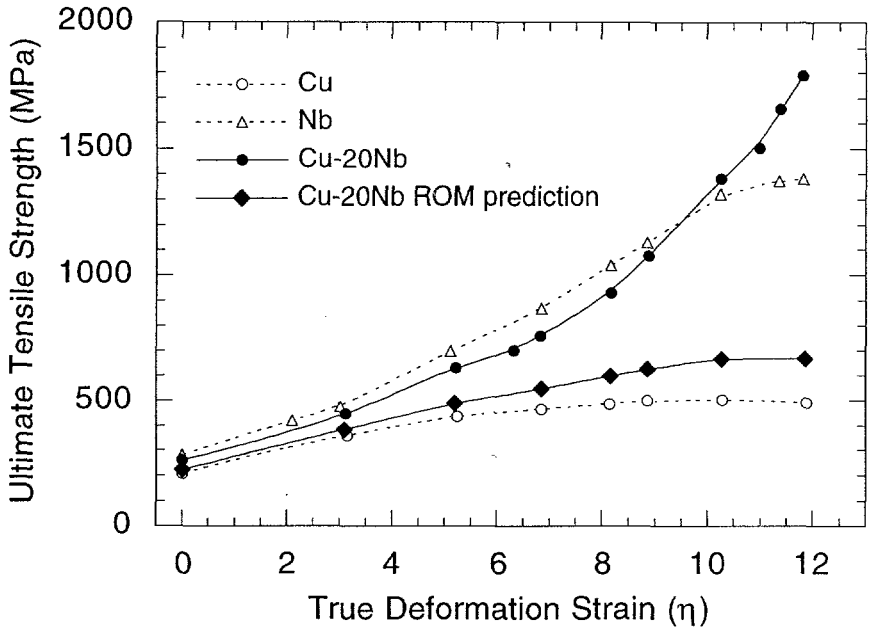

Figure 1. Tensile strength of Cu, Nb, and Cu-20Nb wire related to deformation strain and compared to the ROM predictions [24].

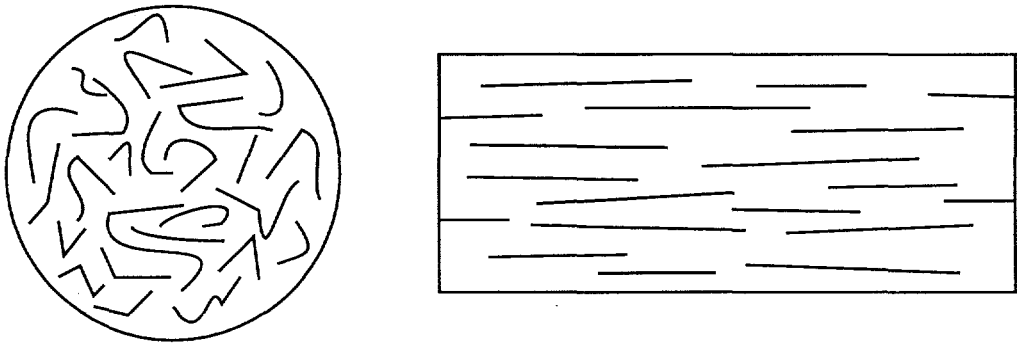

Figure 2. Schematic representation of a typical transverse section of DMMC rod (left) and sheet (right).

high aspect ratios and the microstructure can be classified as being a continuously reinforced composite material. Figure 3 shows a TEM micrograph of heavily deformed Cu-20Nb wire with the folded-ribbon morphology. The ribbon-shaped filaments result from the development of specific textures in the matrix and/or fiber phases during deformation which limit the deformation of the phase to plane strain and will be discussed in more detail later.

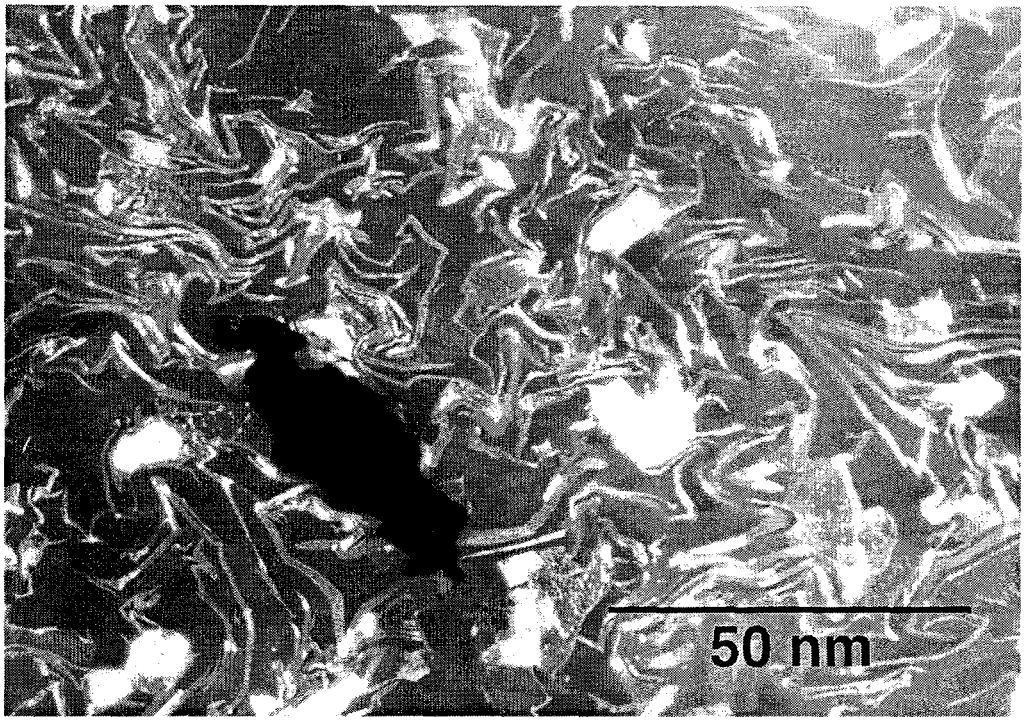

Figure 3. Dark-field conical scan TEM micrograph showing the transverse cross-section of Cu-20Nb wire deformed to $\eta = 12$. The Nb filaments (light) have been refined from an average thickness of 5 μm (at $\eta = 0$) to 7 nm (at $\eta = 12$) in the Cu matrix (dark).

Ti-Y Composites

In an effort to extend the use of deformation processing to non-cubic systems, researchers have studied HCP/HCP Ti-Y composite materials [11-14]. A Ti-20Y composite was deformation processed to a strain of $\eta = 12.8$ by extrusion and drawing with 700°C stress relief anneals performed after each 60% reduction in area. The composite displayed a progressively finer microstructure with increasing amounts of deformation. The as-cast microstructure was characteristic of two immiscible metals (Figure 4).

Deformation changed the original dendritic microstructure to a filamentary structure similar to that observed in Cu-X DMMC materials. The size and spacing of the ribbon-shaped filaments decreased with continuing deformation, resulting in a nanoscale filamentary microstructure (Figure 5) with an average Y phase thickness of 41 nm at $\eta = 7.27$.

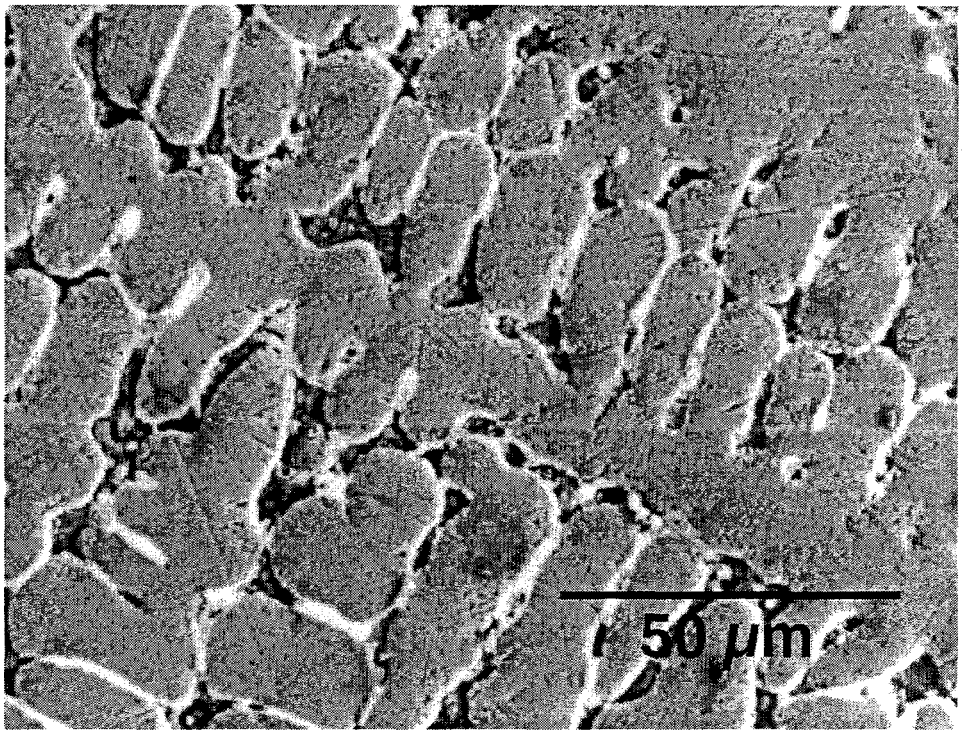

Figure 4. SEM micrograph of as-cast Ti-20Y. The interdendritic Y phase was preferentially removed by the polishing agents.

Figure 5. TEM micrograph of Ti-20Y wire at $\eta = 7.27$ (transverse section).

At the highest levels of deformation ($\eta > 9$), the Ti and Y phases developed an equiaxed grain structure that resulted from recrystallization during periodic stress relief anneals. Annealing was required to prevent the wire from breaking during further cold working. However, the large surface area of the matrix and fiber phases provided a large driving force for recrystallization during annealing. Further deformation produced the filamentary structure previously observed, but the strength of the material did not increase significantly.

Deformation processing more than tripled the UTS of the Ti-20Y composite wire drawn to $\eta = 7.27$ (Figure 6), where the folded-ribbon microstructure was observed. At higher values of η, the phases recrystallized into approximately equiaxed grains and the strength decreased. Ductilities were relatively high for all the Ti-20Y specimens, ranging from 36% to 63% reduction in area at the fracture surface. The Y second phase also improved the machinability of the Ti-20Y composite as compared to pure Ti. The Ti-20Y machining characteristics were qualitatively similar to those of mild steel.

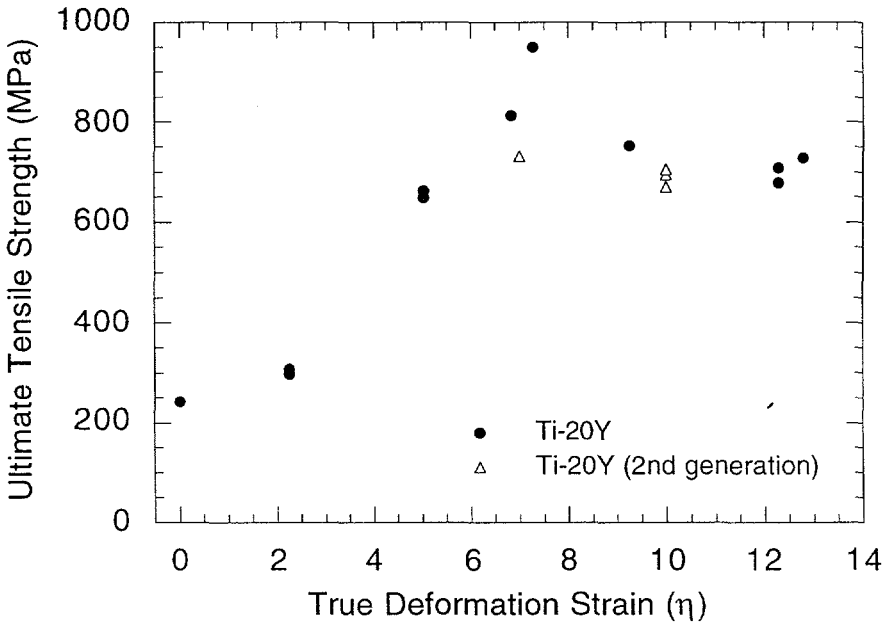

Figure 6. Tensile strength of Ti-20Y wire deformed at room temperature with periodic 700°C anneals. The second generation material was hot worked at 700°C to $\eta = 5.7$ and then cold worked with 600°C anneals.

Texture Development in Ti-Y and Cu-X Composites

X-ray texture pole figures taken on the as-cast Ti-20Y showed no significant texture. However, a pronounced $< 10\bar{1}0 >$ fiber texture was observed in transverse sections of the deformed rod materials for both the Ti and Y phases throughout the deformation range $2.25 \leq \eta \leq 7.27$. The $< 10\bar{1}0 >$ fiber texture is normally observed in drawn Ti [25]; its occurrence in drawn Y has been less thoroughly studied but seems a likely texture for Y since it has a c/a ratio identical to that of Ti [26].

In Cu-Nb DMMC rod materials, the BCC Nb phase typically develops a <110> fiber texture while the Cu matrix develops a <111> and/or <001> fiber texture [27-30]. In a BCC crystal with a <110> fiber texture, two of the four <111> directions ($[1\bar{1}1]$ and $[\bar{1}11]$) are positioned perpendicular to the fiber axis and thus cannot slip. All slip is limited to the remaining two <111> directions ([111] and $[11\bar{1}]$) which lie opposite one another across the specimen center line, thus limiting deformation in the BCC phase to plane strain [1, 31]. The FCC Cu matrix, however, can readily deform axisymmetrically with either the <111> or <001> fiber texture, since these orientations possess three and four active slip directions, respectively. The Cu-X DMMC materials are therefore characterized by plane-straining BCC filaments embedded in a Cu matrix with multiple slip systems that can accommodate the limited deformation mode of the fibers.

The axisymmetrically-deforming FCC Cu which surrounds the plane-straining BCC phase constrains the filaments and results in the curling effect seen in Figure 3. That is to say, the overall specimen geometry remains cylindrical during deformation and so the ribbon-shaped filaments must swirl around the axis of deformation to comply with the deformation of the bulk material. Thus, for an equivalent amount of deformation, FCC/BCC Cu-X DMMC materials have a much thinner effective filament thickness and a much larger matrix/fiber interfacial area than do FCC/FCC deformation processed composites such as Ag-Cu or Ag-Ni. The deformation processed Ag-Cu wire of Frommeyer and Wassermann was comprised of

100% FCC phases which both deform axisymmetrically, and these specimens achieved much lower maximum UTS values (1250 to 1400 MPa) even at filament thicknesses as small as 12 to 25 nm [32]. It has been suggested that the presence of a plane straining phase resulting in the convoluted microstructure seen in Cu-Nb is one of the reasons for the superior strength of the FCC/BCC DMMC materials [1].

There is a striking similarity between the arrangement of available slip systems in an HCP crystal with a $< 10\bar{1}0 >$ fiber texture and in a BCC crystal with a <110> fiber texture. Both situations limit slip to two directions which are bisected by the center line of the rod (as compared to the three or four slip directions possible in a textured FCC lattice), so both crystals are limited to a plane strain deformation mode. This analysis would predict that a DMMC material comprised of HCP metals would undergo the same filament shaping processes that have been observed in the BCC filaments of Cu-X composites. Since both the Ti and Y phases are limited to plane strain in a $< 10\bar{1}0 >$ fiber texture orientation, the folded-ribbon shape seen in the BCC filaments of Cu-X composites would be expected for both phases in the Ti-Y composite. This, in fact, has been observed in Ti-20Y composite wires [11-14].

The exceptionally large interfacial boundary area inherent in such plane-straining microstructures (as seen in Cu-X and Ti-Y) might also explain the anomalous strengthening observed in FCC/BCC Cu-X composites but absent in FCC/FCC composites such as Ag-Cu [32]. The increase in strength observed for the Ti-20Y composite in Figure 6 is quite similar to that observed in the Cu-20Nb composites over the range $0 \leq \eta \leq 7.27$ [1, 4].

As previously mentioned, the Ti-20Y composites did not maintain the desired folded-ribbon microstructure at strains greater than $\eta = 7.27$. This was unfortunate, since the greatest improvement in the mechanical properties of Cu-X composites occurred at the highest true strains where filament thicknesses were reduced to less than 10 nm. The Ti-20Y specimens either recrystallized when high annealing temperatures were used or broke apart during deformation when lower annealing temperatures were used [11-14]. One possible explanation

for the observed inability of the Ti-20Y composite to tolerate very large strains is the geometric challenge of fitting two plane straining phases into a cylinder whose radius diminishes as deformation progresses. It may simply be impossible to fit two plane-straining, ribbon-shaped phases into a contiguous, void-free cylindrical arrangement at high true strains [13, 16].

Mg-X Composites

Mg is mutually immiscible with Ti, Nb, and Fe, and Mg-X composites of these materials were prepared by mixing elemental powders and then pressing the blended powders into a compact suitable for deformation processing. Initial hot working was followed by cold working with periodic stress relief anneals and this deformation changed the original microstructure of the powder compacts into a filamentary structure aligned to the rod axis. As deformation continued, the composites displayed progressively finer microstructures and the strength increased modestly (Figure 7) [16].

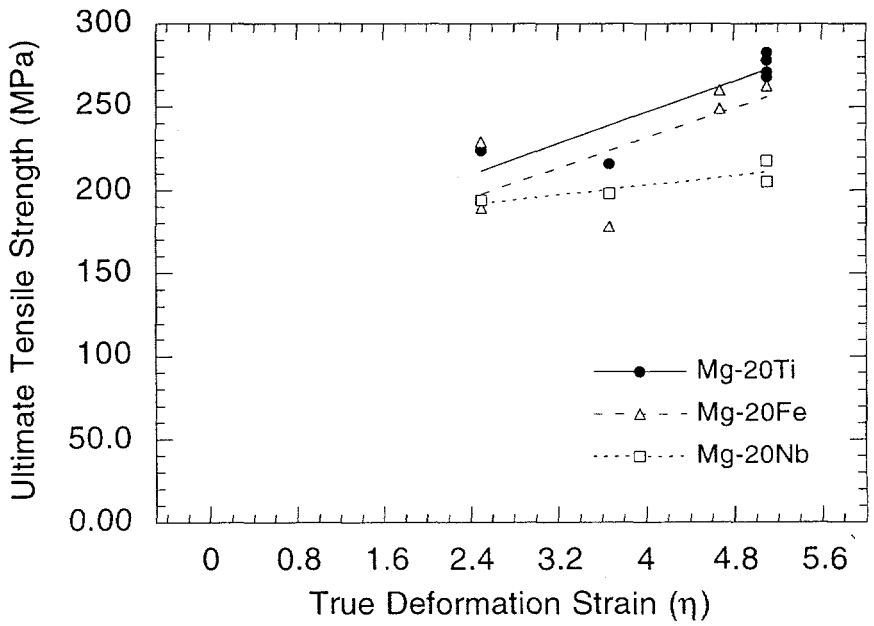

Figure 7. Tensile strength of Mg-X binary alloys deformation processed by extrusion and swaging.

A particularly significant finding from the study of the Mg-X composites was their resistance to microstructural change and loss of strength from exposure to elevated temperatures. Mg-20Ti and Mg-20Nb specimens exposed to temperatures ranging from 300°C to 400°C for 6 to 500 hours showed no change in microstructure (Figure 8) and no loss of ultimate tensile strength (Figure 9). The potential for producing a DMMC material that can be used in high-temperature environments remains the "holy grail" of current Mg-alloy research, but the results from the Mg-X composites provide scientists with some hope of success.

Anticipated Benefits of Deformation-Processed Mg Composites

DMMC research provides an alternate strategy for developing light-weight commercial materials: produce fiber-reinforced composites by heavily deforming a mixture of two ductile metallic phases. DMMC materials offer several potential advantages over conventional metal matrix composites: high strength, good ductility, good formability, good machinability, good matrix/fiber bonding (metallic bonding), high fracture toughness, high temperature stability, and post-forming strengthening (e.g. precipitation hardening or solid state transformations) to improve the properties of the matrix and/or fiber phases in the composite material. Successful development of DMMC materials offers the potential for improving the performance of light metal alloys used in structural applications.

As stated previously, commercial magnesium alloys rely primarily on solid solution strengthening and precipitation hardening. The use of deformation processing to produce fiber-reinforced composite materials with the advantages listed above would represent a true paradigm shift for the light metals industry. The development of lightweight DMMC materials has the potential to revolutionize worldwide commercial applications through improved performance and economic benefits.

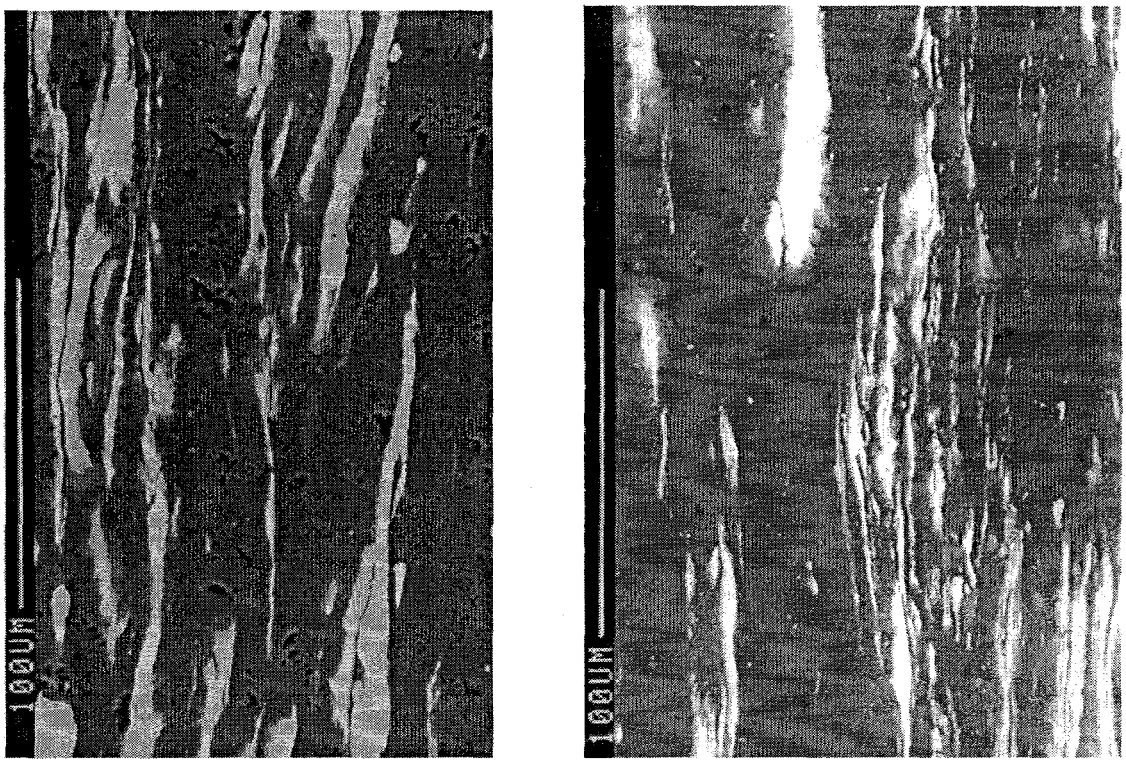

Figure 8. Mg-20Ti rod deformed to $\eta = 5.1$ before (left) and after (right) annealing at in vacuum at 400°C for 6 hours (longitudinal sections).

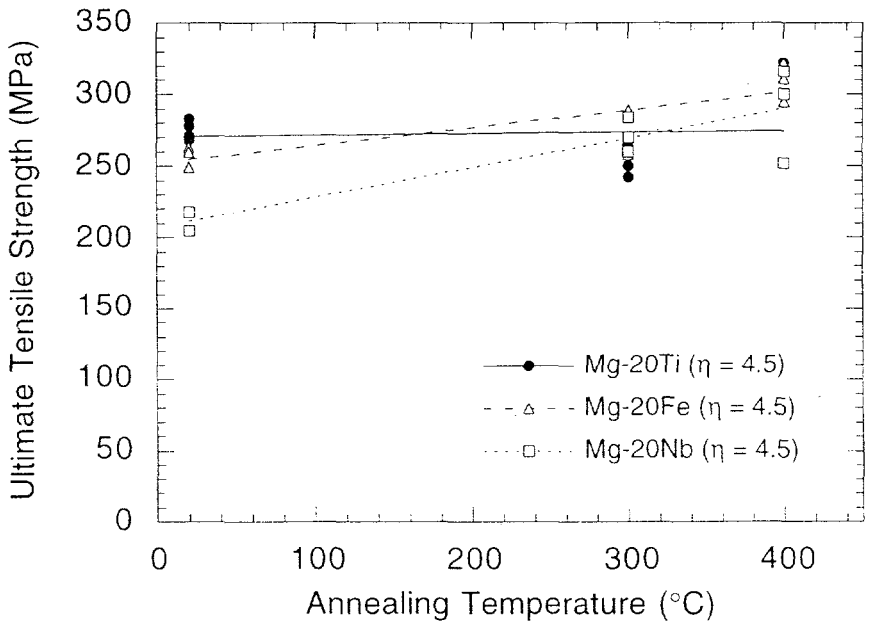

Figure 9. Room temperature strength of Mg-X composites after annealing at 300°C for 24 hours or at 400°C for 500 hours.

Dissertation Organization

This dissertation is written in an alternate format composed of original manuscripts, preceded with general introduction and conclusion chapters. References cited within each chapter have been placed immediately after the chapter.

The first manuscript, presented in Chapter 2, "Processing and Mechanical Properties of Magnesium-Lithium Composites Containing Steel Fibers," was submitted to *Metallurgical and Materials Transactions* in 1997. The authors were Jeff Jensen (graduate student and primary researcher) and Scott Chumbley (graduate advisor), both associated with the Materials Science and Engineering Department at Iowa State University and the Ames Laboratory of the U.S. Department of Energy (DOE) . This manuscript presents an alternative processing method developed to produce castings of the DMMC materials studied and the mechanical properties of these composites.

The second manuscript, presented in Chapter 3, "Microstructure of Magnesium-Lithium Composites Containing Steel Fibers," will be submitted to the *Journal of Materials Engineering and Performance* in 1997. The authors are Jeff Jensen (primary researcher), Scott Chumbley, and Fran Laabs, who assisted with the research. Mr. Laabs is associated with the Ames Laboratory (DOE). This manuscript relates the observed microstructure to the mechanical properties of the heavily deformed DMMC materials.

The third manuscript, presented in Chapter 4, "Texture Development in Magnesium-Lithium Composites Containing Steel Fibers," will be submitted to *Acta Materialia* in 1997. The authors are Jeff Jensen (primary researcher), Fran Laabs, and Scott Chumbley. This manuscript relates the texture development in the matrix and fiber phases to the processing and properties of the DMMC materials.

The fourth manuscript, presented in Appendix A, "Strength of a Heavily Deformed Cu-20Nb Composite," will be submitted to the *Journal of Materials Engineering and Performance* in 1997. The authors are Jeff Jensen (primary researcher), Scott Chumbley, and Andrew

Kuznetsov, a visiting scientist from the Institute of Metal Physics of the Russian Academy of Sciences in Russia who assisted with the mathematical analyses presented in this manuscript.

A fifth manuscript, presented in Appendix B, "Quantitative Fiber Size Measurements for a Theoretical Composite Sheet," was authored by Jeff Jensen. The manuscript is included as a reference describing the difference between stereologically measured fiber sizes and the actual fiber dimensions in a theorietical composite sheet material as a function of deformation.

Additional appendices include raw data from stereology measurements, tensile tests, and some additional SEM and TEM micrographs.

References

1. J. D. Verhoeven: *Fundamentals of Physical Metallurgy*, Wiley & Sons, New York, NY, 1975, pp. 515-519.

2. J. Bevk, J. P. Harbison, and J. L. Bell: *J. Appl. Physics*, 1978, vol. 49(12), pp. 6031-6038.

3. J. D. Verhoeven, L. S. Chumbley, F. C. Laabs and W. A. Spitzig: *Acta metall.*, 1991, vol. 39(11), pp. 2825-2834.

4. J. D. Verhoeven, W. A. Spitzig, L. L. Jones, H. L. Downing, C. L. Trybus, E. D. Gibson, L. S. Chumbley, L. G. Fritzmeier, and G. D. Schnittgrund: *J. Mater. Engineering*, 1990, vol. 12(2), pp. 127-139.

5. C. L. Trybus: *Microstructure-strength relationships of heavily deformed Cu-based composites*, Iowa State University, Ames, Iowa, Ph.D. dissertation, 1988.

6. W. A. Spitzig and P. D. Krotz: *Acta Metall.*, 1988, vol. 36(7), pp. 1709-1715.

7. W. A. Spitzig, A. R. Pelton, and F. C. Laabs: *Acta metall.*, 1987, vol. 35, pp. 2427-2442.

8. J. D. Verhoeven, F. A. Schmidt, E. D. Gibson, and W. A. Spitzig: *JOM*, 1986, vol. 38(9), pp. 20-24.

9. J. D. Verhoeven, W. A. Spitzig, F. A. Schmidt, and C. L. Trybus: *Mat. & Mfg. Proc.*, 1989, vol. 4(2), pp. 197-209.

10. J. D. Verhoeven, W. A. Spitzig, F. A. Schmidt, P. D. Krotz, and E. D. Gibson: *J. of Mat. Sci.*, 1989, vol. 24, pp. 1015-1020.

11. A. M. Russell: *Microstructure-strength relationships of a deformation processed titanium-yttrium composite*, Iowa State University, Ames, IA, Ph.D. dissertation, 1994.

12. A. M. Russell, T. W. Ellis, and L. S . Chumbley: *J. Mater. Sci.*, 1995, vol. 30, pp. 2070-2076.

13. A. M. Russell, L. S. Chumbley, T. W. Ellis, F. C. Laabs, B. Norris, and G. E. Donizetti: *J. Mater. Sci.*, 1995, vol. 30, pp. 4249-4262.

14. A. M. Russell, J. A. Jensen, L. S. Chumbley, D. G. Konitzer, and T. W. Ellis: *Titanium '92: Science and Technology*, ed. F. Froes and I. Caplan, TMS, Warrendale, PA, 1993, pp. 407-414.

15. J. A. Jensen, A. M. Russell, T. W. Ellis, and L. S. Chumbley: *Aluminum and Magnesium for Automotive Applications*, ed. J. D. Bryant and D. R. White, TMS, Warrendale, PA, 1996, pp. 173-187.

16. J. A. Jensen, A. M. Russell, T. W. Ellis, and L. S. Chumbley: *Light Metals 1995*, ed. J. Evans, TMS, Warrendale, PA, 1995, pp. 1367-1374.

17. W. Johnson and P. B. Mellor: *Engineering Plasticity*, Van Nostrand Reinhold, New York, NY, 1973, pp. 109-110.

18. S.W. Tsai and H.T. Hahn, *Intro. to Composite Materials*, Technomic, Lancaster, PA, 1980, pp. 381-388.

19. P. D. Funkenbusch and T. H. Courtney: *Scripta metall.*, 1989, vol. 23, pp. 1719-1724.

20. W. A. Spitzig, J. D. Verhoeven, C. L. Trybus and L. S. Chumbley: *Scripta metall.*, 1990, vol. 24, pp. 1171-1174.

21. P. D. Funkenbusch and T. H. Courtney: *Scripta metall.*, 1989, vol. 24, pp. 1175-1180.

22. W. A. Spitzig, J. D. Verhoeven, C. L. Trybus and L. S. Chumbley: *Scripta metall.*, 1990, vol. 24, pp. 1181-1182.

23. P. D. Funkenbusch and T. H. Courtney: *Scripta metall.*, 1989, vol. 24, pp. 1183-1184.

24. W. A. Spitzig: *Acta metall.*, 1991, vol. 39(6), pp. 1085-1090.

25. G. Y. Chin: *ASM Metals Handbook*, 1985, vol. 8, 8th ed., pp. 229-232.

26. A. I. Pikalov, V. V. Vorob'yev, I. I. Papirov, and A. S. Kapcherin: *Izv. Akad. Nauk SSSR, Metally*, 1983, vol. 4, pp. 153-156.

27. A. R. Pelton, F. C. Laabs, W. A. Spitzig, and C. C. Cheng: *Ultramicroscopy,* 1987, vol. 22, pp. 251-266.

28. J. D. Verhoeven, W. A. Spitzig, L. L. Jones, H. L. Downing, C. L. Trybus, E. D. Gibson, L. S. Chumbley, L. G. Fritzmeier, and G. D. Schnittgrund, *J. Mat. Engr.*, 1990, vol. 12(2), pp. 127-139.

29. C. L. Trybus: *Microstructure-strength relationships of heavily deformed Cu-based composites*, Iowa State University, Ames, Iowa, Ph.D. dissertation, 1988.

30. Morris and Morris: Acta metall., 1991, vol. 39(8), pp. 1763-1770.

31. W. F. Hosford, Jr., *Trans. Met. Soc. AIME* , 1964, vol. 230, pp. 12-15.

32. G. Frommeyer and G. Wassermann, *Acta metall.*, 1975, vol. 23, pp. 1353-1360.

33. J. D. Embury, *Scripta metall.*, vol. 27, 1992, pp. 981-986.

APPENDIX A: STRENGTH OF A HEAVILY DEFORMED Cu-20Nb COMPOSITE

J. A. Jensen*, A. Kuznetsov**, L. S. Chumbley*

* Ames Laboratory (DOE) and the Department of Materials Science and Engineering
Iowa State University, Ames, IA 50011

** Institute of Metal Physics of the Russian Academy of Sciences
18 S. Kovalevskaya Street, Yekaterinburg 620219, Russia

Abstract

Heavily deformed Cu-20 vol% Nb sheet and wire have strengths which greatly exceed rule-of-mixtures predictions. While the strengthening mechanisms have been debated, experimental data clearly show that the strength increases as the Nb filament thickness and Cu channel spacing decrease during deformation. Empirical models relating the strength to the observed filament size and spacing have been developed based on the Hall-Petch relationship and the Gil Sevillano model. However, these analyses have failed to properly evaluate the effect of σ_0, the friction stress. Assumptions that σ_0 is zero or that σ_0 ranges from 386 MPa to 653 MPa are inconsistent with the description of σ_0 found in the literature. While determining a value for σ_0 is elusive, the effect of this parameter on the empirical models is substantial and must be considered in any analysis of the strengths of these materials. This paper examines TEM and mechanical properties data for Cu-20Nb wire while considering the effects of σ_0 on the strengthening models.

Introduction

In situ composites or deformation-processed metal-matrix composites (DMMC) prepared by extensively deforming a mixture of two immiscible ductile phases constitute an interesting class of materials due to their anomalous high strengths [1-3]. Models have been proposed to correlate the observed mechanical properties of these materials with microstructural features such as dislocations or filament spacings [4-6]. While controversy has existed regarding the strengthening mechanism(s) in these composites [7-11], it has been clearly shown that strength increases as the filament size and spacing decreases [1-6]. Consequently, the role the filaments must play in the development of high strengths in these materials is significant and empirical relationships have been developed to describe strength as a function of filament size and spacing [4-6].

Work on a Cu-20 vol% Nb (Cu-20Nb) DMMC deformed by cold rolling or wire drawing reported that the strengthening effect produced by the filaments depended on the type of deformation [2]. Two distinct differences were noted. Firstly, the overall strength of the rolled composite was lower for a given filament size and spacing than the strength of the wire drawn material. By considering the Schmid factors and the texture development during deformation, it can be shown that an effective filament spacing for sheet material exists which is longer than a simple measurement of the average filament spacing [12]. The second difference concerns the increase in ultimate tensile strength (UTS) with decreasing filament spacing as measured with optical, scanning electron, or transmission electron microscopy (OM, SEM, TEM). The strength was modeled in these studies with a Hall-Petch relationship with an exponent ranging from 0.38 to 0.45 for wire drawn material [2, 3] and 0.27 for sheet material [2]. Differences in the exponent were related to the resolution of the measuring technique used [3]. However, the general trend shown in these studies, namely, a difference in the strengthening observed in sheet versus wire material, seems to be valid. It is the intent

of this paper to re-examine the data produced by earlier studies in an attempt to resolve some of the questions that remain concerning the strengthening of these heavily deformed materials.

Background

The most significant work published that relates the strength of Cu-20Nb composites to microstructural features is found in [2] and [3]. A typical microstructure of a Cu-20Nb composite wire is shown in Figure 1a. The microstructure consists of Cu channels of width λ and Nb filaments of width t, as illustrated in Figure 1b. Using SEM measurements of λ and t, UTS data for Cu-20Nb wire were fit with a Hall-Petch equation and yielded the exponents stated above. The strengthening of the wire was explained as following a simple Hall-Petch type relationship since the exponent fell reasonably close to the 0.5 value predicted by that theory. The failure of the best-fit curve for the sheet material to exhibit a slope of 1/2 as predicted by Hall-Petch was interpreted in [2] to mean that some substructural feature of the Cu matrix was controlling the strength of the sheet material (e.g. dislocation cell walls or deformation twins) rather than the Cu channel size or Nb filament thickness.

A comparison of the SEM data for Cu-20Nb wire in [2] to the TEM data in [3] showed conclusively that the SEM data overestimated the average values of λ and t at high deformation levels. SEM and TEM micrographs of identical regions in a TEM sample of Cu-20Nb wire at $\eta = 9.8$ (where η is the true deformation strain; $\eta = 2 \ln(d_0/d)$ and d_0 and d are the initial and final diameters, respectively) demonstrated the resolution limitations of the SEM. In one region of the sample, the SEM showed what appeared to be a single Nb filament approximately 400 nm thick. Using the TEM, the same microstructural feature was determined to consist of 19 Nb filaments with an average thickness of 7.5 nm. Since SEM measurements were shown to yield significant errors at deformation levels of $\eta > 3$, only TEM data for $\eta > 4$ were used in [3] for purposes of establishing empirical relationships.

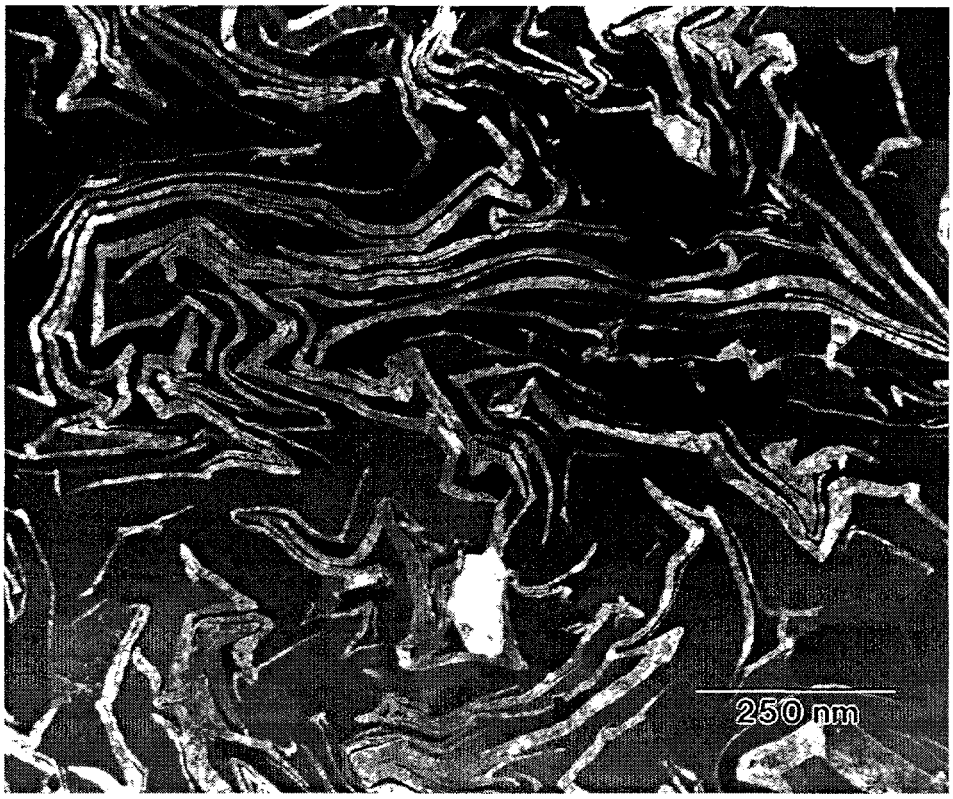

(a)

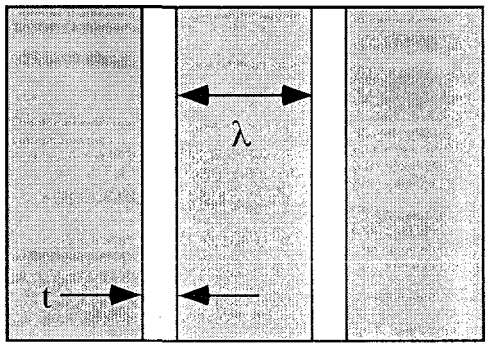

(b)

Figure 1. (a) Typical microstructure from a Cu-20Nb composite wire (TEM, conical scan dark field, transverse section). (b) Schematic illustrating the measured values of λ and t. Cu is dark; Nb is light.

Although TEM measurements of Cu-20Nb wire at $\eta < 4$ were also reported in [3], the data were not used for one of several reasons. Firstly, OM and SEM observations at low η levels indicated the presence of many large Nb filaments which were not visible in the TEM [3]. Consequently, SEM measurements tend to overestimate phase sizes at high η values while TEM measurements tend to underestimate phase sizes at low η values. Secondly, extrapolating TEM data to low η values does not give the known starting dendrite size. This is a direct result of the quantitative stereology methods used, where the measured filament size is related to the shape, orientation, and distribution of the second phase. This makes it difficult to quantitatively compare the irregular, bulky shape of dendrites to the shape of aligned, ribbon-shaped filaments [13]. Since transition from the dendritic structure to a uniformly aligned ribbon-shaped structure was completed at $\eta \approx 3$, TEM data for $\eta > 4$ is valid for modeling the strength of the Cu-20Nb wire.

By using more accurate TEM measurements, it was shown in [3] that the Hall-Petch exponent changed from 0.45 to 0.38 (Figure 2). Thus, the strength of Cu-20Nb wire did not follow the Hall-Petch relationship and the data was re-analyzed using the Gil Sevillano model [19]. The Gil Sevillano equation was modified in [3] using a rule-of-mixtures (ROM) approach to account for both Cu and Nb phase sizes and UTS was used instead of yield stress. The wire data was seen to correspond well with this theory, although no attempt was made to explain the strengthening effect seen in the sheet material in terms of the Gil Sevillano model.

Results and Discussion

The well-known Hall-Petch equation that describes strengthening as a function of barrier spacing is:

$$\sigma = \sigma_0 + kd^{-n} \qquad (1)$$

where n = 1/2 (ideal), σ is the UTS, σ_0 is the friction stress, d is the filament size or spacing,

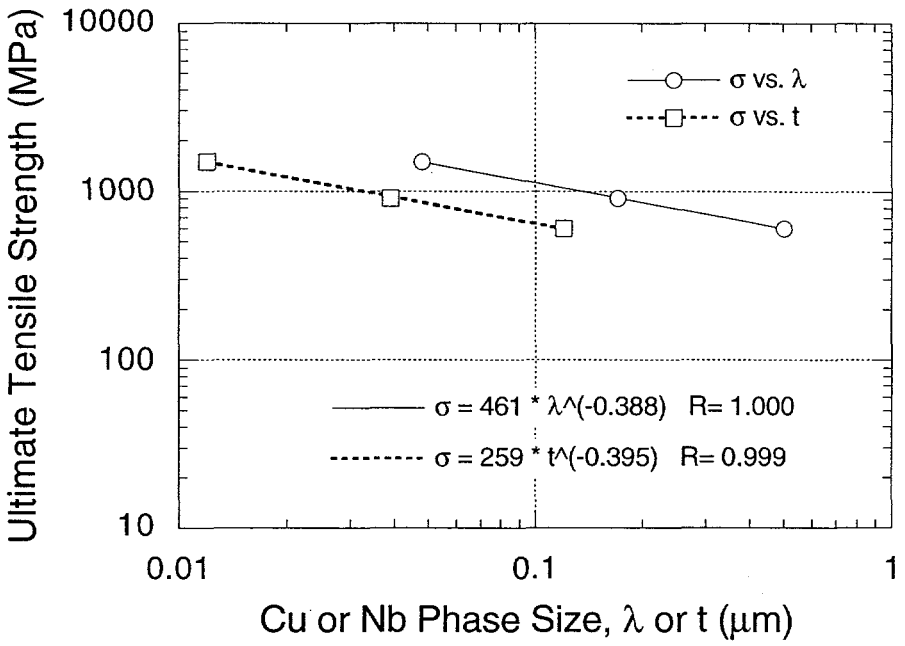

Figure 2. UTS as a function of λ and t for Cu-20Nb wire using TEM measurements and assuming σ_0 is zero).

and k is an empirical fitting parameter [15]. The theory of Gil Sevillano also predicts that strength will increase as barrier spacing decreases, according to the relation:

$$\sigma_c = \sigma_0 + \frac{MAGb}{2\pi d} \ln \frac{d}{b} \qquad (2)$$

where σ_c is the critical stress necessary to propagate dislocations between lamellae, M is the Taylor factor (M = 3 in FCC metals, M = 2 in BCC metals), A = 1.21 for mixed dislocations, G is the shear modulus, b is the Burgers vector, d is the barrier spacing (λ or t), and σ_0 is the friction stress [19]. Note that both the Hall-Petch and Gil Sevillano models contain the term σ_0. There is considerable confusion as to the physical meaning of this parameter. Perhaps the most honest definition of σ_0 was given by Hull and Bacon [23] who stated that σ_0 was "a constant stress of uncertain origin." Given the presence and importance of σ_0 in both models, a brief review of this parameter is appropriate.

Derivation of σ_0

Hall [21] and Petch [22] take σ_0 to be the extrapolated y-intercept value for plots of the lower yield point of a single crystal or fracture stress of a polycrystalline material, respectively, versus the inverse square root of grain size. Hertzberg [18] defines σ_0 in the Hall-Petch equation as the friction stress, which is a measure of "lattice resistance to dislocation movement resulting from various strengthening mechanisms and intrinsic lattice friction (Peierls stress)." Referring specifically to lath martensite, Norstrom [14] proposed a comprehensive relation describing yield strength:

$$\sigma_{YS} = \sigma_P + k\sqrt{c} + \alpha Gb\sqrt{\rho} + k_y d^{-1/2} \tag{3}$$

where σ_{YS} is the yield strength, σ_P is the Peierls stress, $k\sqrt{c}$ is solid solution strengthening, $\alpha Gb\sqrt{\rho}$ is strain hardening, and $k_y d^{-1/2}$ is boundary hardening. In this equation the first three terms of the summation ($\sigma_P + k\sqrt{c} + \alpha Gb\sqrt{\rho}$) correspond to σ_0. Conrad [17] stated that σ_0 was a summation of two separate terms, σ_{ST} which is sensitive to the structure of the material and varies with the type of strengthening mechanism and σ_T which is sensitive to testing temperature. A general equation which accounts for each of these strengthening mechanisms would have the form:

$$\sigma_0 = \sigma_P + \sigma_{ss} + \sigma_{sh} + \sigma_{ppt} \tag{4}$$

where σ_0 is the friction stress, σ_P is the Peierls stress, σ_{ss} is solid solution strengthening, σ_{sh} is strain hardening, and σ_{ppt} is precipitation strengthening.

One might think of σ_0 as the Peierls stress for an imperfect single crystal. It includes the Peierls stress for the perfect crystal plus the cumulative effects of solid solution strengthening, strain hardening, and precipitation strengthening. One only needs to calculate the Peierls stress in order to solve for σ_0. The Peierls stress is generally assumed to be constant for a given compound or elemental crystalline arrangement and only two known

variations in the Peierls stress appear possible. The first is the well documented variation of the Peierls stress with temperature [15, 17, 18, 22] and the second is related to the width of a dislocation in a given crystalline lattice. The temperature effect can be discounted for this study since all mechanical testing was done at room temperature. However, the effect of dislocation width on the Peierls stress is difficult to quantify.

The Peierls stress is considered to be an intrinsic lattice friction required to move a dislocation through a crystalline lattice. Attempting to determine an exact value for the Peierls stress from first principles is difficult. For example, Foreman *et al.* [24] have shown that minor variations in calculations of the Peierls stress can change the computed value by six orders of magnitude! Hirth and Lothe [15] have discussed the displacement potential (related to the Peierls stress discussed here) at great length. In [15], the model that was first derived by Peierls and later extended by Nabarro was shown to be useful in determining the width and core energy of a dislocation. However, [15] states that "the extension of the model to predict the lattice displacement potential resisting dislocation motion rests on quite tenuous assumptions." Refinements of the Peierls-Nabarro model have been developed by many theorists, but [15] shows that consideration of such refinements is of questionable value in view of the uncertainties in the Peierls model. Hirth and Lothe describe the shortcomings of the original Peierls-Nabarro solution and show several refinements to the original model; however, all of the models qualitatively retain the basic assumption of the original Peierls-Nabarro work and retain the corresponding degree of uncertainty.

Hirth and Lothe [15] state that even though there are large uncertainties in all of the quantitative predictions of the Peierls energy barrier, the predictions all agree that the Peierls energy should decrease as the dislocation width, planar spacing, and temperature increase, and that the Peierls energy should be lower for edge dislocations than for screw dislocations. The corollary to the first generalization indicates that the force required to move a dislocation increases as the width of the dislocation decreases. Hirth and Lothe [15] conclude that the

maximum value of the periodic lattice resistance stress is the Peierls stress, σ_P, which should be regarded as a phenomenological parameter.

Attempts have been made to determine an exact value for the Peierls stress from first principles. All of the model predictions suffer from a large degree of uncertainty [15, 24]. However, experiments [15] indicate that σ_P varies from approximately $10^{-4}\mu$ to $10^{-2}\mu$ (where μ is the shear modulus), with higher values associated with covalent crystals and lower values associated with close-packed metals. For Cu and Nb, the shear moduli are 48.3 and 37.5 GPa, respectively, and ROM calculations predict the corresponding σ_P to be on the order of 5 to 500 MPa for Cu-20Nb.

Determination of σ_0 for Cu-20Nb

To determine σ_0 for Cu-20Nb one must consider the collective effects of the Peierls stress, solid solution strengthening, strain hardening, and precipitation strengthening. Since the impurity levels in the as-cast ingot were low, and Cu and Nb are mutually immiscible, the effect of impurity strengthening on σ_0 must be low. The same reasoning would also apply to precipitation strengthening effects: with no impurities present and no miscibility, no precipitates should form. Indeed, no precipitates have ever been observed in the numerous TEM investigations of this material. One can calculate the maximum contribution of hardening due to dislocation pile-ups in Cu using the following equation from [25]:

$$\Delta\sigma_{Cu} = \left(\frac{Gb}{4}\right)\left(\sqrt{\rho_2} - \sqrt{\rho_1}\right) \tag{5}$$

where $\Delta\sigma_{Cu}$ is the increased strength due to a higher dislocation density, G = shear modulus (= 48.3 GPa for Cu), b = Burgers vector (= 0.26 nm for Cu), ρ_1 is the initial dislocation density, and ρ_2 is the final dislocation in the material. Using the dislocation densities reported in [26] for as-cast and highly deformed wire and sheet material yields a maximum hardening

effect of ≈70 MPa in the Cu phase. Similar values can be obtained for $\Delta\sigma_{Nb}$, so a rule of mixtures approach will not vary significantly from the calculated hardening effect for pure Cu. The effect due to increased dislocation densities in Cu-20Nb is, therefore, small compared to the overall strength of the material at high deformation levels.

In the Hall-Petch analyses of [2] and [3], a value of zero was used for σ_0. If $\sigma_0 = 0$ then dislocations could move freely and indefinitely without any applied stress. Thus, $\sigma_0 = 0$ is a poor assumption and σ_0 must have some finite value. In the Gil Sevillano analysis of [3], σ_0 for the Cu-20Nb composite at any given η was taken to be the weighted average of the UTS for pure Cu and pure Nb deformed to the same strain. This results in a σ_0 which is a function of deformation strain, as would be expected from the σ_{sh} term in Equation 4. According to the derivation in [3], σ_0 would increase from 225 MPa (as-cast) to 670 MPa at the highest levels of deformation sustained by the material. Over the range of deformation modeled in [3], σ_0 varied from 386 to 653 MPa. Calculations based on dislocation densities observed in the TEM (above) show that σ_0 should only increase 70 MPa as a result of strain hardening. If these calculations are true, then the values for σ_0 used in [3] are in error.

In Figure 3 below, the TEM data of [3] have been evaluated using a constant value of $\sigma_0 = 225$ MPa, obtained by calculating the weighted average of the UTS for pure Cu (209 MPa) and pure Nb (275 MPa) in the annealed condition [20]. Using this value of σ_0 the Hall-Petch exponent was determined to be 0.52, rather than 0.38, as reported in [3]. Note: fitted equations include the correlation coefficient, R, which ranges from 0 (poor fit) to 1 (ideal fit).

Figure 4 shows the Gil Sevillano UTS predictions of [3], labeled $\sigma_0 = f(\eta)$ to show that σ_0 was a function of deformation, and those using a fixed σ_0 value of 225 MPa. The solid line indicates ideal agreement with this model. With a fixed value for σ_0, the Gil Sevillano model now significantly underestimates the strength of the Cu-20Nb wire. It is interesting to note that the Hall-Petch model correlates well with the data when σ_0 is assumed to be constant, while the Gil Sevillano model describes the data equally well when σ_0 varies as

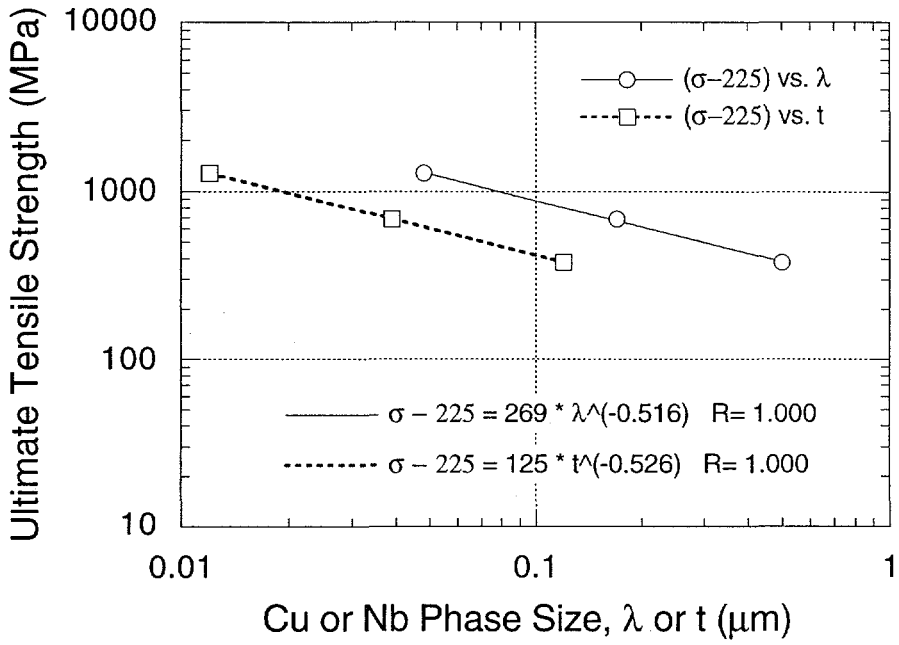

Figure 3. UTS as a function of λ and t for Cu-20Nb wire using TEM measurements and assuming σ_0 = 225 MPa.

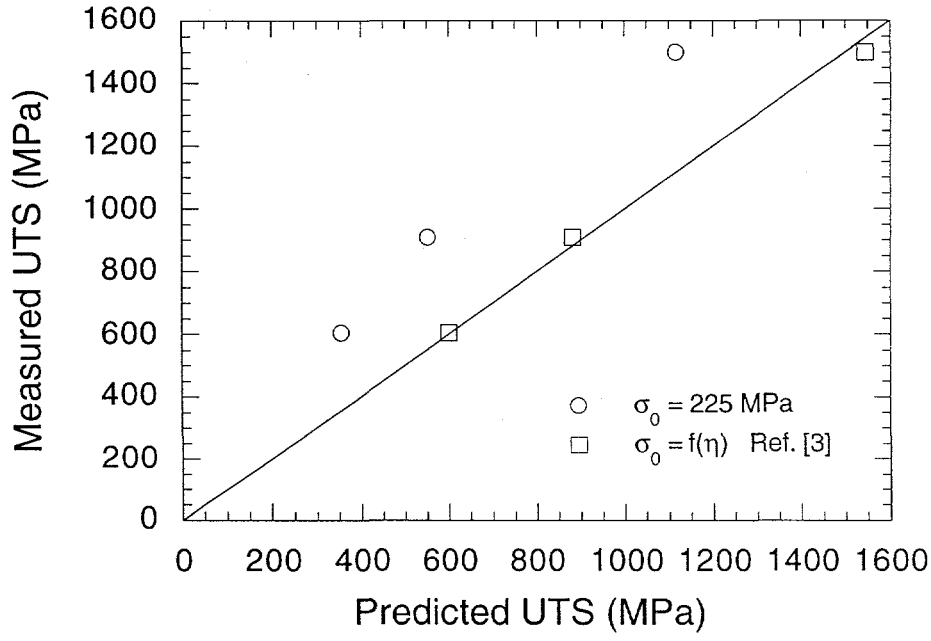

Figure 4. Gil Sevillano UTS predictions using TEM measurements for Cu-20Nb wire.

a function of deformation. Thus, depending on the assumed value of σ_0, both models are equally valid for describing the strengthening observed in Cu-20Nb wire.

These analyses show that σ_0 plays an instrumental role in determining how well the data can be modeled. The value of 225 MPa used in this study seems reasonable; however, other approaches to determining σ_0 may be equally valid. It might be argued that the as-cast UTS of the starting ingot could be considered as a good approximation to σ_0 since this equals the stress necessary to move a dislocation through the Cu-Nb structure before the aligned microstructure develops. The as-cast UTS was experimentally determined to be 250 MPa [2, 3], which is close to the 225 MPa value for σ_0. Fitting the TEM data of [3] with the Hall-Petch relationship and assuming $\sigma_0 = 250$ MPa yields an exponent of 0.54 with a correlation of $R = 0.999$.

Another value for σ_0 can be determined from Equation 4. Although this equation contains several terms, only σ_P and the strain hardening term (σ_{sh}) need to be considered for Cu-20Nb. Calculations showed (Equation 5) that a maximum σ_{sh} value of 70 MPa is expected. Assuming that σ_0 increases linearly from 250 MPa to 320 MPa to account for strain hardening, the Hall-Petch exponent was determined to be 0.52 with a correlation of $R = 1.000$ (Figure 5). A value for σ_0 can also be determined if one assumes that the ideal Hall-Petch equation applies to Cu-20Nb wire (i.e. $n = 1/2$) and plots UTS versus $d^{-1/2}$ (where $d = \lambda$ or t). Figure 6 shows that the y-intercepts of these lines yield an average σ_0 value of 200 MPa.

These analyses show that all reasonable values for σ_0 result in an excellent Hall-Petch correlation between the tensile strength and observed filament spacings in Cu-20Nb wire. However, the Gil Sevillano model applied successfully in [3] does not work well if $\sigma_0 = 225$ MPa (Figure 4). Assuming a value of $\sigma_0 = 200$ MPa, or that σ_0 ranges from 250 to 320 MPa, produces similar results; i.e. measured UTS data are higher than predicted UTS values (Figure 7). Thus, the Gil Sevillano does not apply to Cu-20Nb wire when σ_0 is evaluated correctly.

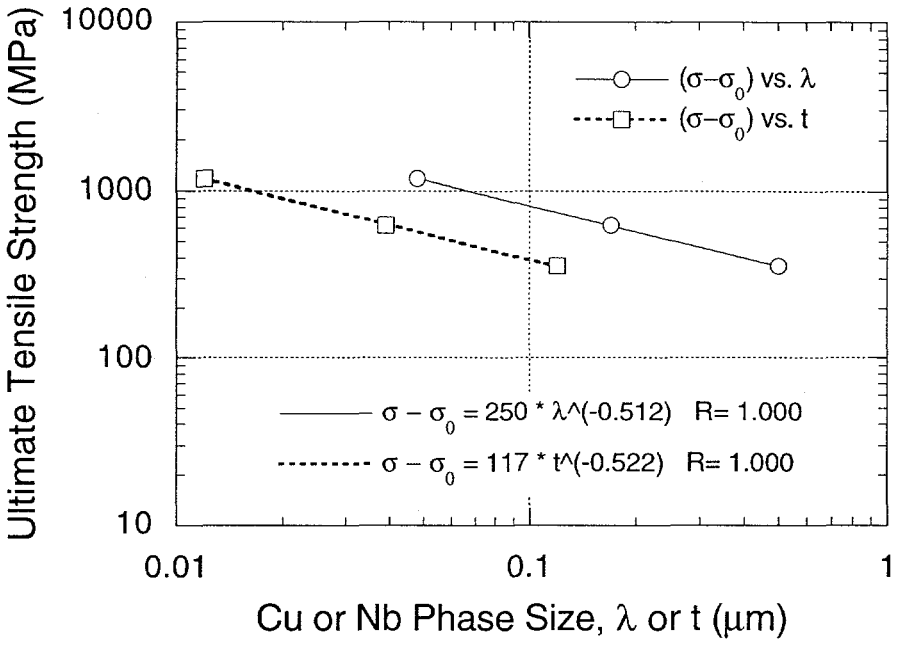

Figure 5. UTS as a function of λ and t for Cu-20Nb wire using TEM measurements and assuming that σ_0 increases from 250 to 320 MPa.

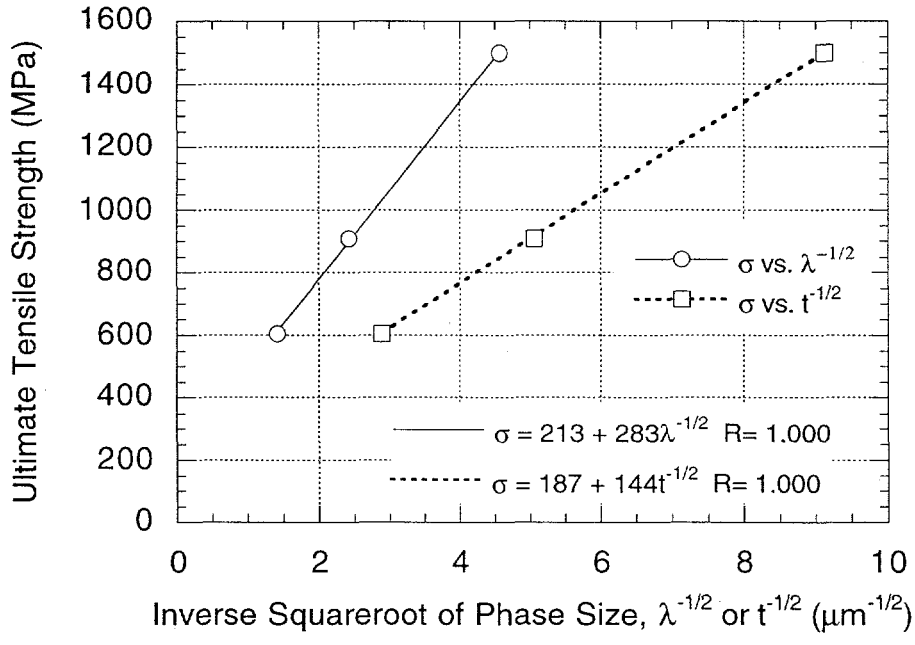

Figure 6. Determination of σ_0 for Cu-20Nb wire by assuming the ideal Hall-Petch relationship (i.e. n = 1/2) and using d = λ or t.

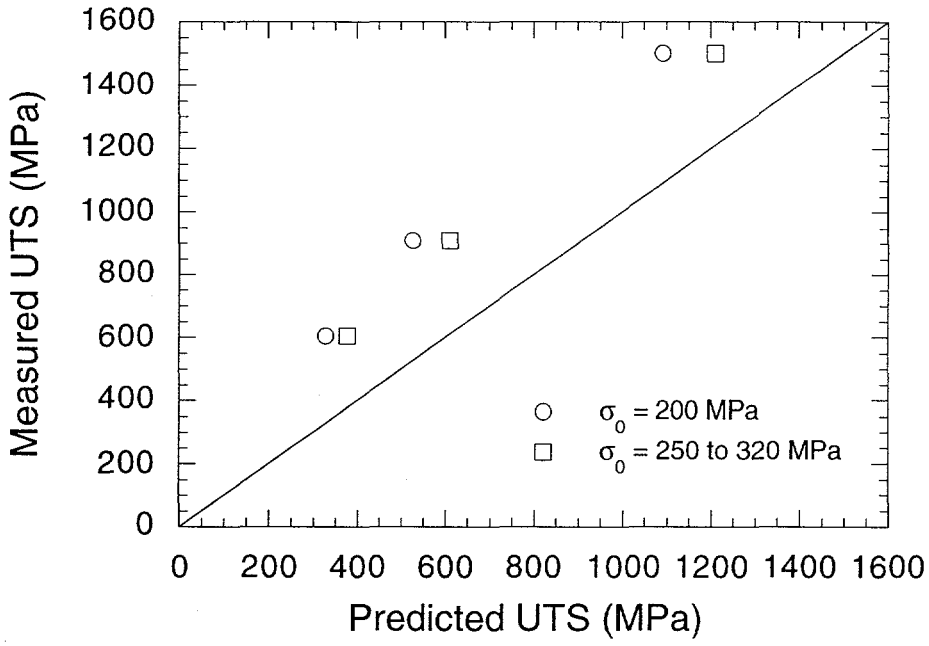

Figure 7. Gil Sevillano UTS predictions using TEM measurements for Cu-20Nb wire.

The Gil Sevillano and Hall-Petch models both predict that the strength of a material will increase when the barrier spacing is decreased. However, these models assign different weights to this barrier spacing effect. For example, the Hall-Petch model shows that strength increases with $(\sqrt{d})/d$, where d is the barrier spacing, while the Gil Sevillano model predicts that the strength increases as a function of $\ln(d/b)/d$, where b is the Burgers vector. Thus, the Gil Sevillano model has a stronger dependence on barrier spacing than the Hall-Petch model. As shown in Figures 3-6, both models can be used to describe the strengthening seen in Cu-20Nb wire, depending on the choice of σ_0 and the constant associated with the barrier spacing factor. For example, the weaker barrier spacing dependence of the Hall-Petch model can be overcome by the fitting parameters (σ_0 and k) determined for the experimental data.

Although both models can be forced to fit the UTS data for Cu-20Nb wire, the Gil Sevillano model applied in [3] uses a range of values for σ_0 that assumes a large strain hardening effect that is not confirmed by TEM measurements of dislocation densities. The

combination of the strong dependence on barrier spacing and the choice of large values for σ_0 in [3] increased the strength predictions of the Gil Sevillano model enough to fit the strength data for the Cu-20Nb wire. On the other hand, the Hall-Petch analyses described in this paper accurately describe the strengthening observed in Cu-20Nb wire while using values for σ_0 which agree with other evidence such as dislocation densities, the estimated Peierls stress, the predicted ROM strength of the composite in the annealed condition, and the as-cast strength of the composite. The results of this study indicate that the use of any particular strengthening model must be carefully evaluated in regard to all available physical data and that only reasonable assumptions are used.

Finally, it should be noted that Embury and Fisher [27-28] also developed a Hall-Petch type of relationship to describe the strength of pearlitic steel wire as a function of deformation. Their model was based on the assumption that the ferrite and cementite phases deformed at the same rate as the bulk material. The Embury-Fisher model has the advantage that one need only measure the initial barrier spacing using SEM or TEM and then calculate barrier spacing as a function of deformation. However, the model is invalid if the internal and external shape changes of the material are not consistent. For example, the barrier spacing in Cu-20Nb wire and sheet [1] and in strip-drawn pearlitic steel [29] is not reduced at the same rate as the deformation of the bulk material, so the basic assumption of the Embury-Fisher is not fulfilled in these systems. Using the Embury-Fisher model for Cu-20Nb wire results in a worse correlation to the experimental data than the Hall-Petch model based on TEM measurements of filament spacing. Thus, this model was not considered relevant for the above analysis.

One final mention should be made of the possible effect the filamentary structure of these composites has on the value of σ_0. TEM studies have shown that the composite microstructure becomes extremely fine at high levels of deformation, with Cu channels (λ) less than 50 nm in width and Nb filaments (t) less than 10 nm in width. Although the literature reports no minimum grain size required for the Hall-Petch relationship to be valid, the

nanoscale microstructures of the nature examined in this study were never considered by Hall and Petch [21-22], and a wide body of literature shows that nanoscale materials have different mechanical properties than similar large-grain materials [30-31]. Depending upon the Burgers vector of the dislocation and the direction of movement, this fine microstructure may limit the width a dislocation can assume and/or prevent additional dislocations from being generated. Experimental studies which have shown that dislocation generation and motion in finely spaced lamellar structures becomes difficult, if not impossible, resulting in large strength increases [32-33]. This type of strengthening mechanism may alter the Peierls stress (σ_P) or require an additional term to be added to the summation for σ_0 (Equation 4). This strengthening mechanism was not considered since the Hall-Petch model accurately describes the strength of Cu-20Nb wire. However, if the size and spacing of the filaments was further decreased, one might need to consider the nanoscale strengthening effects described in [32-33].

Summary and Conclusions

It has been shown that previous theoretical analyses used to explain the strengthening seen in heavily deformed Cu-20Nb wire failed to properly consider and evaluate the effect of σ_0, the stress associated with lattice resistance to dislocation motion and internal friction effects. Assumptions that $\sigma_0 = 0$ or that σ_0 varies from 386 MPa to 653 MPa do not agree with the description of σ_0 presented in the literature or with other experimental data such as TEM measurements of dislocation densities. The influence of σ_0 on the Hall-Petch exponent (Table I) and on the Gil Sevillano predictions make this an important parameter to consider in any theoretical treatment. Depending on the values chosen for σ_0, it is conceivable that many models could be used to explain the strengthening observed in Cu-20Nb wire and sheet. However, the assumptions required for the Gil Sevillano model to fit the Cu-20Nb wire data do not seem reasonable, while the Hall-Petch model accurately describes the observed strengthening in a manner which agrees with other data available for this composite.

Table I. Parameters Determined for Hall-Petch Model, $\sigma = \sigma_0 + kd^{-n}$

Figure	d =	Assumed σ_0 (MPa)	k	n	R
2	λ	0	461	0.388	1.000
2	t	0	259	0.395	0.999
3	λ	225	269	0.516	1.000
3	t	225	125	0.526	1.000
	λ	250	248	0.536	0.999
	t	250	112	0.547	1.000
5	λ	250-320	250	0.512	1.000
5	t	250-320	117	0.522	1.000
	λ	320	192	0.605	0.999
	t	320	78	0.617	1.000
7	λ	213*	283	0.50*	1.000
7	t	187*	144	0.50*	1.000

* Assumed n = 1/2 and determined σ_0 and k.

Acknowledgments

The authors would like to thank F. C. Laabs for his valuable assistance and J. D. Verhoeven for helpful discussions. This work was performed for the U.S. Department of Energy at the Ames Laboratory, Iowa State University, under contract No. W-7405-Eng-82. The research was supported by the Director of Energy Research (Office of Basic Energy Sciences), the Office of Naval Research Graduate Fellowship Program, and the International Institute of Theoretical and Applied Physics.

References

1. C. L. Trybus, *Microstructure-strength relationships of heavily deformed Cu-based composites*, Iowa State University, Ames, Iowa, Ph.D. dissertation, 1988.

2. C. L. Trybus and W. A. Spitzig, *Acta metall.*, 1989, vol. 37, pp. 1971-1981.

3. J. D. Verhoeven, L. S. Chumbley, F. C. Laabs and W. A. Spitzig, *Acta metall.*, 1991, vol. 39(11), pp. 2825-2834.

4. W. A. Spitzig, *Acta metall.*, 1991, vol. 39(6), pp. 1085-1090.

5. W. A. Spitzig, A. R. Pelton, and F. C. Laabs, *Acta metall.*, 1987, vol. 35, pp. 2427-2442.

6. P. D. Funkenbusch and T. H. Courtney, *Acta metall.*, 1986, vol. 33, pp. 913-922.

7. P. D. Funkenbusch and T. H. Courtney, *Scripta metall.*, 1989, vol. 23, pp. 1719-1724.

8. W. A. Spitzig, J. D. Verhoeven, C. L. Trybus and L. S. Chumbley, *Scripta metall.*, 1990, vol. 24, pp. 1171-1174.

9. P. D. Funkenbusch and T. H. Courtney, *Scripta metall.*, 1989, vol. 24, pp. 1175-1180.

10. W. A. Spitzig, J. D. Verhoeven, C. L. Trybus and L. S. Chumbley, *Scripta metall.*, 1990, vol. 24, pp. 1181-1182.

11. P. D. Funkenbusch and T. H. Courtney, *Scripta metall.*, 1989, vol. 24, pp. 1183-1184.

12. L. S. Chumbley, Ames Laboratory and Iowa State University, Ames, IA, unpublished research, 1988.

13. E. E. Underwood, *Quantitative Stereology*, Addison-Wesley, Reading, MA, 1970, pp. 80-93.

14. L. A. Norstrom, *Scand. J. Metall.*, 1977, vol. 5, p. 159.

15. J. P. Hirth and J. Lothe, *Theory of Dislocations*, McGraw-Hill, New York, NY, 1984, pp. 201-229, 716-717.

16. A. M. Russell, *Microstructure-strength relationships of a deformation processed titanium-yttrium composite*, Iowa State University, Ames, IA, Ph.D. dissertation, 1994.

17. H. Conrad, *JISI*, 1961, vol. 198, p. 364.

18. R. W. Hertzberg, *Deformation and Fracture Mechanics of Engineering Materials*, Wiley & Sons, New York, NY, 1989, p. 133.

19. J. Gil Sevillano, *Strength of Metals and Alloys, Proc. ICSMA 5*, Pergamon Press, Oxford, 1980, ed. P. Haasen, V. Gerold and G. Kowtorz, p. 819.

20. *Properties and Selection: Nonferrous Alloys and Pure Metals, Metals Handbook*, American Society for Metals, Metals Park, OH, 1979, 9th ed. vol. 2, pp. 714-831.

21. E. O. Hall, *Proc. Phys. Soc.*, 1951, vol. B64, p. 747.

22. N. J. Petch, *Phil. Mag.*, 1956, vol. 1, p. 186.

23. D. Hull and D. J. Bacon, *Introduction to Dislocations*, Pergamon Press, Elmsford, NY, 1968, p. 248.

24. A. J. Foreman, M. A. Jaswon, and J. K. Wood, *Proc. Phys. Soc.*, 1951, vol. A64, p. 156.

25. Fridel, *Dislocations*, Pergamon Press, New York, NY, 1964.

26. C. L. Trybus, L. S. Chumbley, W. A. Spitzig, and J. D. Verhoeven, *Ultramicroscopy*, 1989, vol. 30, p. 315.

27. J. D. Embury and R. M. Fisher, *Acta metall.*, vol. 14, 1966, pp. 147-159.

28. J. D. Embury, *Scripta metall.*, vol. 27, 1992, pp. 981-986.

29. G. Langford, *Met. Trans.*, 1977, vol. 8A, pp. 861-875.

30. H. Wilsdorf, O. Inal, and L. Murr: *Z. Metallkunde*, 1978, vol. 69, p. 556.

31. J. Karch, R. Birringer, and H. Gleiter: *Nature*, 1987, vol. 330, p. 556.

32. J. S. Koehler: *Physical Rev.*, 1970, vol. B2, p. 547.

33. D. Tench and J. White: *Metall. Trans.*, 1984, vol. 15A, 2039.

APPENDIX B. QUANTITATIVE FIBER SIZE MEASUREMENTS FOR A THEORETICAL COMPOSITE SHEET

Introduction

The quantitative stereology methods described by Underwood [1] can be used to relate easily measured metallographic parameters to an average fiber diameter called the mean intercept length ($\overline{L}_3$) for single or multi-phase materials. For fibers embedded in a composite material, $\overline{L}_3$ represents the average distance between any two points lying on the surface of a fiber. For particles with simple geometries $\overline{L}_3$ can also be determined mathematically. For example, in spherical particles, $\overline{L}_3$ is equal to two-thirds the diameter . For flat disks and plates such that the thickness is much smaller than the other dimensions of the particle, $\overline{L}_3$ is equal to twice the thickness of the particle. Mathematical and stereological determinations of fiber size estimate the mean intercept length, $\overline{L}_3$, rather than the actual thickness of a ribbon-shaped filament.

Quantitative stereological methods can be used to determine the size and spacing of filaments embedded in a composite material. The mean free distance (λ) between particles is given by:

$$\lambda = (1 - V_f) / N = V_m / N \qquad (1)$$

where V_f is the volume fraction of fibers, V_m is the volume fraction of the matrix, and N is the number of interceptions per unit length of test lines with the fibers. V_f, V_m, and N can be determined by stereological methods, while V_f and V_m can also be determined from chemical analysis or density measurements if uniform particle dispersion is assumed. Equation 1 is supposedly "valid regardless of size, shape, or distribution of particles" and is "essentially the mean edge-to-edge distance" between phases [1]. Since the number of interceptions with the

fibers is the same as the number of interceptions with the matrix, the average thickness of the fibers (t) can be estimated from the following equation:

$$t = (1 - V_m) / N = V_f / N \qquad (2)$$

where V_m is the volume fraction of the matrix. The value for t is actually an equivalent fiber "diameter" that is the average distance between all possible pairs of points lying on the surface of a fiber and is called the mean intercept length, designated as $\overline{L}_3$ in [1].

Some doubt was raised during the analysis of fiber sizes in [2] as to the validity of the measured values for $\overline{L}_3$ (i.e. t), especially for the composite sheet material analyzed with SEM and TEM. The stereologically measured values for the fiber size differed considerably from the fiber thickness predicted from the deformation applied to the bulk composite material and this discrepancy was questioned.

To understand this discrepancy, a theoretical composite sheet material was designed to allow the comparison of the known fiber thickness to the stereologically measured values of $\overline{L}_3$ described above. $\overline{L}_3$ was also calculated from the mathematical descriptions in [1] and compared to the known thickness of the theoretical fibers and the stereologically measured values. Since the composite sheet material studied in [2] is generally thought to have lamellar fibers, the rectangular parallelepiped particle shape was chosen as the mathematical equivalent. For this particle shape, the mean intercept length is given as:

$$\overline{L}_3 = \frac{2abc}{ab + bc + ca} \qquad (3)$$

where a, b, and c are the dimensions of the filament [1].

Procedure and Results

Transverse and longitudinal sections of a theoretical composite material containing 25 volume percent fibers were sketched for deformation strains up to $\eta_e = 4.0$ (96.9% RT), where the effective deformation strain is $\eta_e = (2/\sqrt{3})(\eta)$, the true deformation strain is $\eta = \ln(t_0/t)$, %RT refers to the percent reduction in thickness, and t_0 and t are the initial and final thicknesses of the sheet, respectively. The width of the theoretical sheet material was assumed to remain constant so that deformation produced a reduction in thickness and corresponding increase in length. The matrix and fiber phases were assumed to perfectly codeform in direct proportion to the bulk sheet material. Therefore, during deformation the fibers became longer and thinner while maintaining a constant width. The initial fibers were assumed to be 1 cm x 1 cm x 10 cm. A 10 cm x 10 cm micrograph was sketched at each deformation level and used for stereological measurements that could be compared to the actual and mathematical values for fiber size.

The number of intercepts per length (N) were determined by placing two concentric circles over the micrographs and counting the number of times the circles intersected the fibers. This number was then divided by the known length of the two circles (33 cm originally). The circles and micrographs used to determine N are printed below at a slightly reduced magnification (Figures 2-8). It is assumed that the transverse sections are exactly perpendicular to the rolling direction and that the longitudinal sections lie in the plane defined by the rolling direction and the sheet normal. The dashed line in Figure 2 shows the location of the longitudinal section in relation to the transverse section. Table I shows the results of the measurements and calculations in this theoretical study. In Table I, t_T and t_L refer to $\bar{L}_3$ values determined from Equation 2 using the concentric circles to measure N on micrographs of transverse and longitudinal sections, respectively; t' refers to the value for $\bar{L}_3$ calculated using Equation 3; and t_{actual} is the true fiber thickness assuming that the fibers

perfectly deformed in the composite sheet. Figure 1 plots these fiber size determinations as a function of effective deformation strain.

Note that t_{actual} refers to the thickness of the individual filaments while $\overline{L}_3$ refers to a fiber "diameter" equivalent to the average length between all possible pairs of points on the surface of a filament. As suggested in [1], when a << b and a << c then $\overline{L}_3$ can be estimated by 2a (i.e. twice the filament thickness). This can be seen at $\eta_e = 4.00$, where t' is nearly twice the value of t_{actual}. Also note that the values for t_T and t_L begin to converge at higher levels of deformation. In general, $\overline{L}_3$ for any flat particle (ribbon, flat disc, square plate, etc.) is equal to twice the thickness of the particle, provided that the thickness is small in comparison to the other particle dimensions.

Discussion

Researchers often consider the thickness of the filaments when heavily deforming a composite material and predict the fiber thickness based on the deformation of the bulk material. Stereological measurements of the fiber size are often completed and then reported as being in disagreement with the "actual" (i.e. predicted) fiber size. One must be careful when comparing stereological measurements of $\overline{L}_3$ to the actual fiber thickness, especially when the fiber size is used to model the strengthening behavior of the material. Researchers must remember that the filament thickness is usually not the same as "mean intercept length" described by $\overline{L}_3$, which represents a three-dimensional equivalent fiber "diameter" [1]. For example, in heavily deformed DMMC sheet materials, the stereologically determined fiber size exceeds the actual filament thickness by a factor of two at high levels of deformation. Certainly some data reported in the literature should be corrected in light of the stereological definition of filament size and spacing.

References

1. E. E. Underwood: *Quantitative Stereology*, Addison-Wesley, Reading, MA, 1970, pp. 80-93.

2. J. A. Jensen: *Microstructure-strength relationships of heavily deformed magnesium-lithium composites containing steel fibers*, Iowa State University, Ames, IA, Ph.D. dissertation, 1997.

Tables and Figures

Table I. Determining $\bar{L}_3$ for a Theoretical Composite Sheet

%RT	η	η_e	b (cm)	c (cm)	$a = t_{actual}$ (cm)	$\bar{L}_3$		
						t_T (cm)	t_L (cm)	t' (cm)
0	0	0	1	10	1.0	0.8250	1.650	0.9524
50.0	0.69	0.80	1	20	0.5	0.5500	0.7500	0.6557
75.0	1.39	1.60	1	40	0.25	0.3173	0.4125	0.3980
87.5	2.08	2.40	1	80	0.125	0.1750	0.1964	0.2219
93.75	2.77	3.20	1	160	0.0625	0.09167	0.09821	0.1176
96.88	3.47	4.00	1	320	0.03125	0.04688	0.04970	0.06060

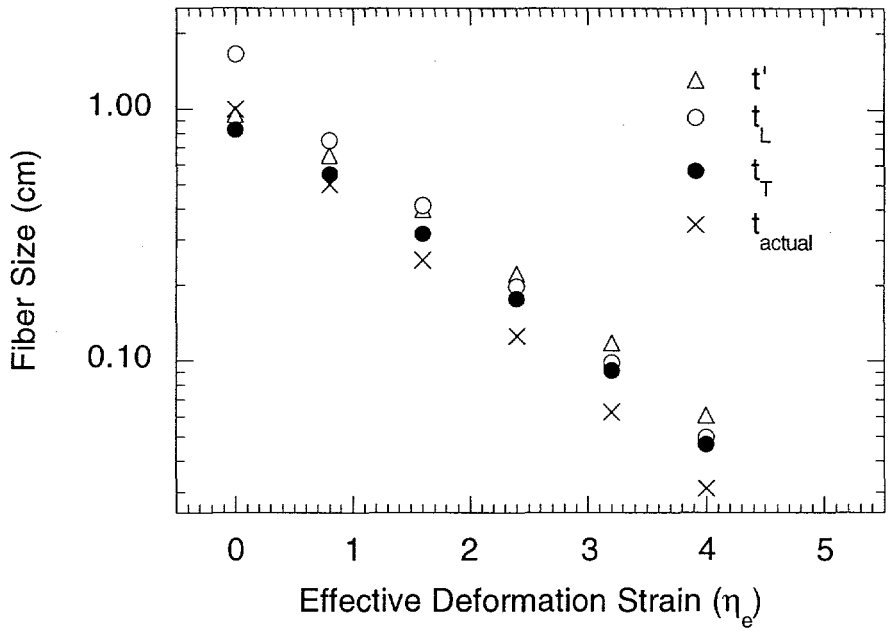

Figure 1. Fiber size determinations: stereologically measured on micrographs of transverse (t_T) and longitudinal (t_L) sections, calculated from stereological formulas (t'), and the actual fiber thickness.

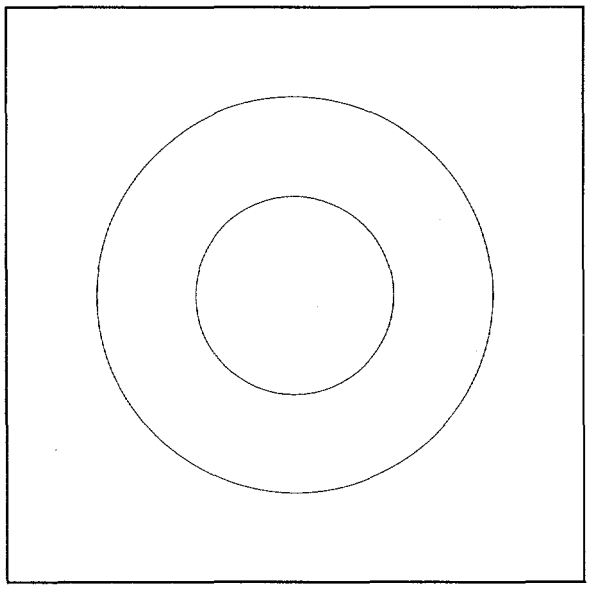

Figure 2. Concentric circles used to determine the number of intercepts per length (N) for the theoretical composite sheet.

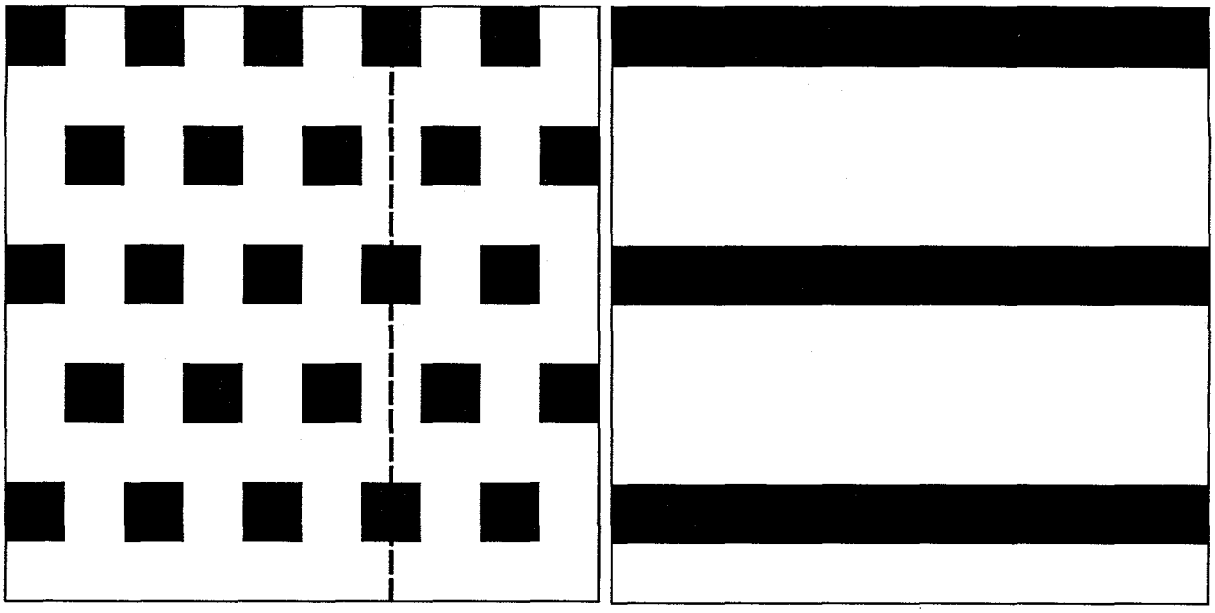

Figure 3. Original theoretical composite sheet containing 25 vol% fibers. The dashed line on the transverse section (left) shows the plane used for longitudinal (right) measurements. Fibers were 1 cm x 1 cm x 10 cm and magnification was 1x before the sketches were reduced for printing.

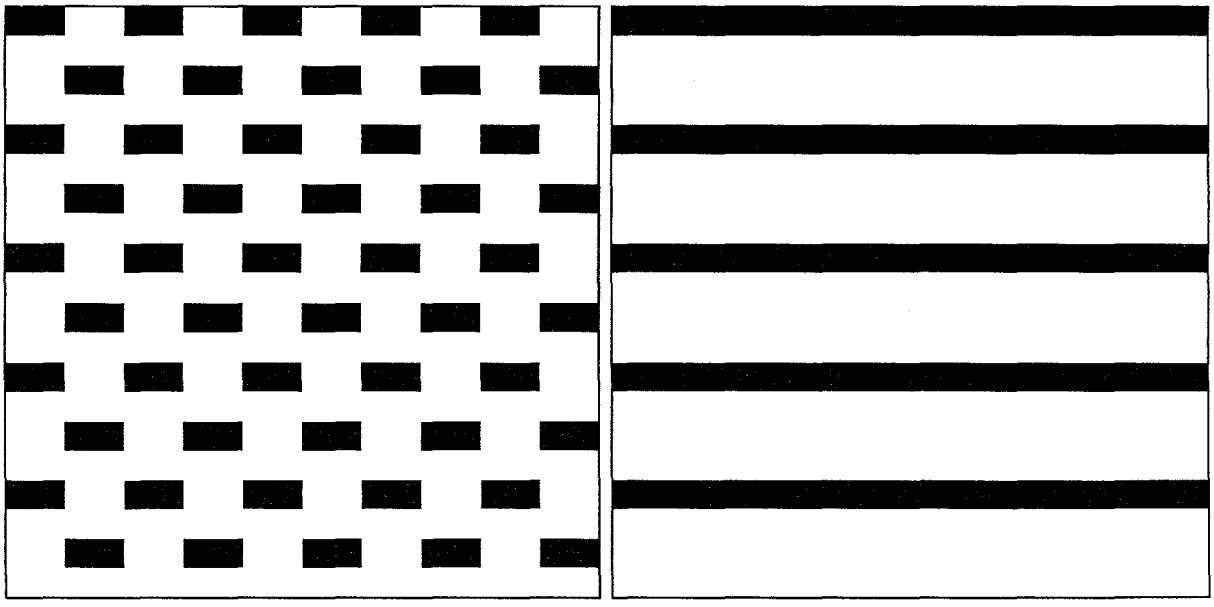

Figure 4. Theoretical composite sheet rolled to 50% RT showing transverse (left) and longitudinal (right) sections. Fibers were 0.5 cm x 1 cm x 20 cm and magnification was 1x before the sketches were reduced for printing.

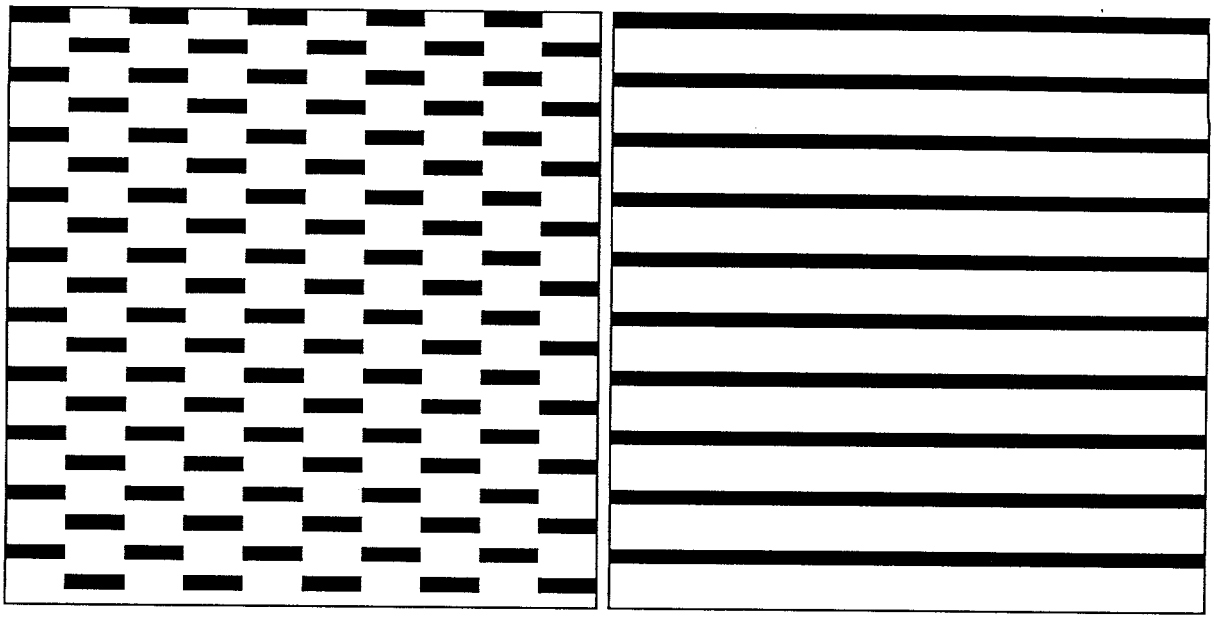

Figure 5. Theoretical composite sheet rolled to 75% RT showing transverse (left) and longitudinal (right) sections. Fibers were 0.25 cm x 1 cm x 40 cm and magnification was 1x before the sketches were reduced for printing.

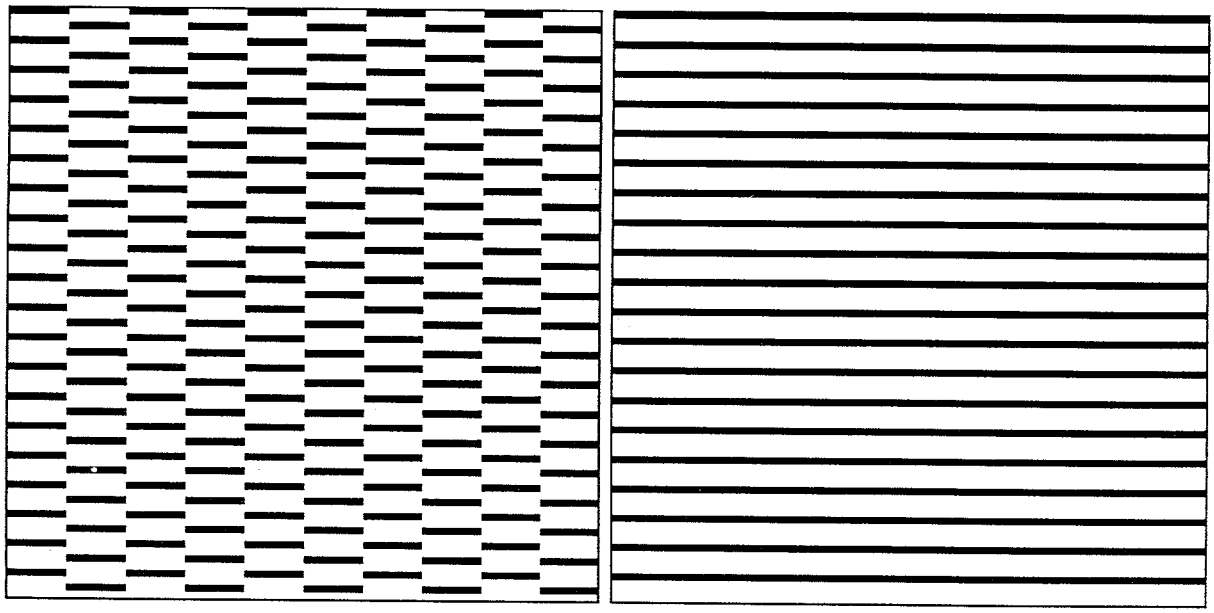

Figure 6. Theoretical composite sheet rolled to 87.5% RT showing transverse (left) and longitudinal (right) sections. Fibers were 0.125 cm x 1 cm x 80 cm and magnification was 1x before the sketches were reduced for printing.

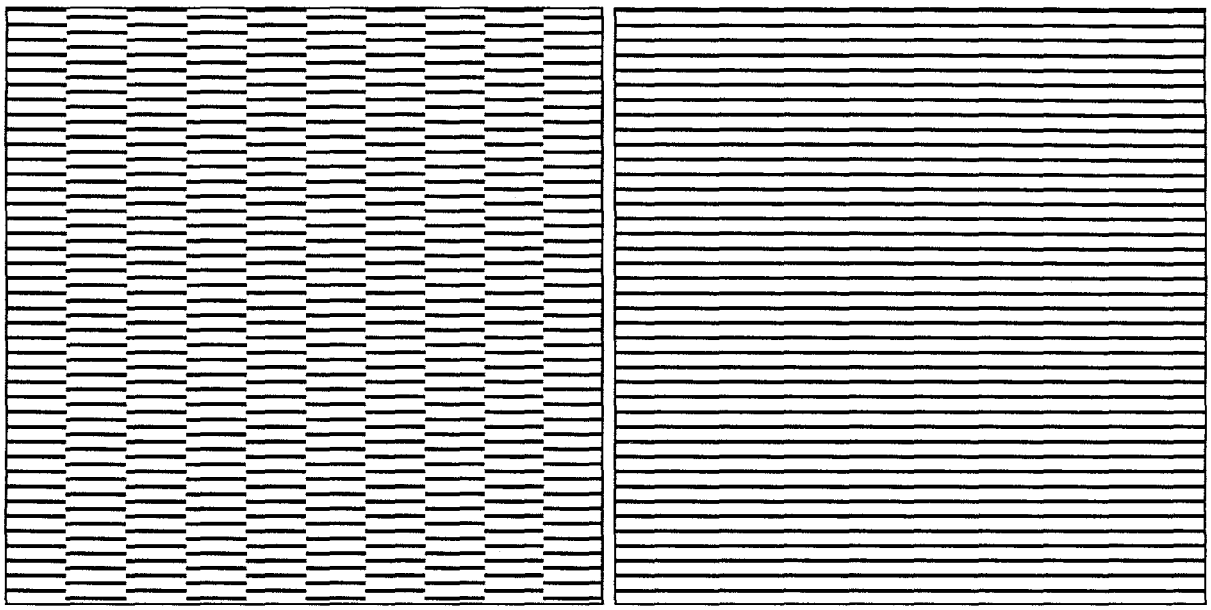

Figure 7. Theoretical composite sheet rolled to 93.75% RT showing transverse (left) and longitudinal (right) sections. Fibers were 0.0625 cm x 1 cm x 160 cm and magnification was 1x before the sketches were reduced for printing.

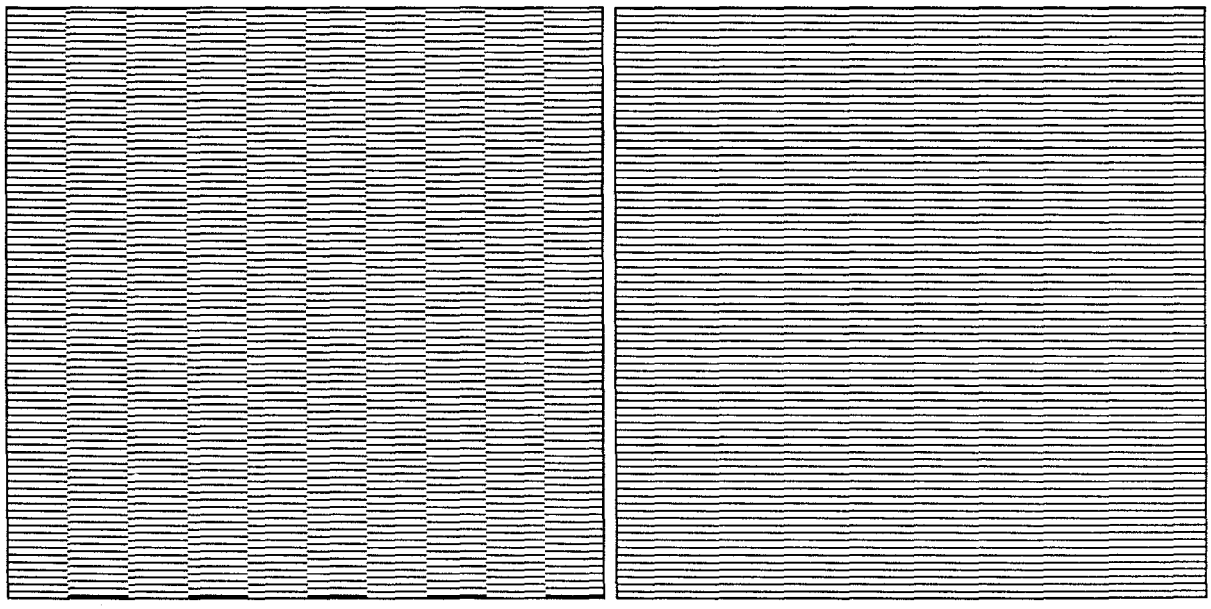

Figure 8. Theoretical composite sheet rolled to 96.88% RT showing transverse (left) and longitudinal (right) sections. Fibers were 0.03125 cm x 1 cm x 320 cm and magnification was 1x before the sketches were reduced for printing.

APPENDIX C. SIZE AND SPACING OF FIBERS IN Mg-Li/Fe COMPOSITES

Table C1. Nomenclature Used in Appendix C.

Symbol	Description
pic#	number assigned to each micrograph
scope	microscope used to acquire the micrograph: scanning electron microscope (SEM) or transmission electron microscope (TEM)
mag	magnification of the original micrograph
orient	orientation of the SEM or TEM sample: normal (N), longitudinal (L), or transverse (T) section of the composite material
η	true deformation strain
η_e	effective deformation strain (for sheet)
vol fr (ex)	stereologically determined volume fraction of Fe fibers
vol fr (th)	volume fraction of Fe fibers determined from bulk density measurements
N	number of interceptions per unit length for a given phase
λ (ex)	mean free distance between Fe fibers based on vol fr (ex)
λ (th)	mean free distance between Fe fibers based on vol fr (th)
t (ex)	mean intercept length of Fe fibers based on vol fr (ex)
t (th)	mean intercept length of Fe fibers based on vol fr (th)
t (ruler)	average Fe fiber thickness obtained by measuring with a ruler the thickest portion of each fiber visible on a micrograph
min t	smallest observed Fe fiber as measured with a ruler for each micrograph of a material at a given deformation strain
max t	largest observed Fe fiber as measured with a ruler for each micrograph of a material at a given deformation strain
min t observed	smallest observed Fe fiber as measured with a ruler from among all micrographs of a material at a given deformation strain
max t observed	largest observed Fe fiber as measured with a ruler from among all micrographs of a material at a given deformation strain
max/min ratio	ratio of (max t)/(min t)
avg min t observed	average (min t) for all micrographs of a material at a given strain
avg max t observed	average (max t) for all micrographs of a material at a given strain
avg max/min ratio	average (max/min ratio) for all micrographs of a material at a given deformation strain
AVERAGE	average of values indicated
STDEV	standard deviation of values indicated

Table C2. Summary of Stereological Measurements Describing the Mg-4Li/27Fe and Mg-12Li-2Nd/21Fe DMMC Materials

	Strain (η or η_e)	vol fr (ex)	N (cm^{-1})	λ (ex) (μm)	λ (th) (μm)	t (ex) (μm)	t (th) (μm)	t (ruler) (μm)
Mg-12Li-2Nd/21Fe Casting	**0**	**0.27**	**1.02**	**42.92**	**46.52**	**15.96**	**12.37**	**12.24**
STDEV		0.06	0.45	5.25	5.03	3.97	1.34	1.93
Mg-12Li-2Nd/21Fe Sheet	**1.89**	**0.32**	**1.61**	**14.33**	**16.66**	**6.77**	**4.43**	
STDEV		0.06	0.56	3.30	3.27	1.83	0.87	
Mg-12Li-2Nd/21Fe Sheet	**3.67**	**0.30**	**0.52**	**4.60**	**5.23**	**2.02**	**1.39**	**1.29**
STDEV		0.10	0.18	2.03	2.46	1.33	0.65	
Mg-12Li-2Nd/21Fe Sheet	**3.97**	**0.33**	**1.75**	**4.14**	**4.89**	**2.05**	**1.30**	**2.08**
STDEV		0.07	0.74	0.98	0.92	0.54	0.24	0.96
Mg-12Li-2Nd/21Fe Sheet	**5.55**	**0.27**	**1.10**	**1.75**	**1.84**	**0.58**	**0.49**	**0.34**
STDEV		0.05	0.66	1.14	1.07	0.22	0.29	
Mg-12Li-2Nd/21Fe Sheet	**6.5**	**0.30**	**1.37**	**1.53**	**1.65**	**0.68**	**0.44**	**0.63**
STDEV		0.07	0.72	0.73	0.83	0.39	0.22	0.49
Mg-12Li-2Nd/21Fe Rod	**3.07**	**0.34**	**0.59**	**6.93**	**8.19**	**3.45**	**2.18**	
STDEV		0.08	0.38	2.56	2.09	0.72	0.56	
Mg-12Li-2Nd/21Fe Rod	**4.29**	**0.30**	**1.21**	**5.23**	**5.46**	**2.05**	**1.45**	
STDEV		0.07	0.47	1.70	1.39	0.39	0.37	
Mg-12Li-2Nd/21Fe Rod	**5.98**	**0.32**	**0.90**	**2.57**	**2.47**	**0.68**	**0.66**	
STDEV		0.11	0.24	0.75	0.44	0.18	0.12	
Mg-4Li/27Fe Casting	**0**	**0.31**	**0.90**	**40.47**	**36.48**	**16.14**	**13.49**	
STDEV		0.05	0.22	9.57	6.80	5.66	2.52	
Mg-4Li/27Fe Rod	**2.69**	**0.33**	**1.28**	**11.51**	**11.21**	**5.55**	**4.15**	
STDEV		0.04	0.34	2.70	3.21	1.55	1.19	
Mg-4Li/27Fe Rod	**3.92**	**0.30**	**1.32**	**7.86**	**8.16**	**3.31**	**3.02**	
STDEV		0.05	0.33	1.63	1.31	0.34	0.48	

Table C3. Summary of Minimum and Maximum Fe Fibers Observed in Mg-4Li/27Fe and Mg-12Li-2Nd/21Fe DMMC Materials

	Strain (η or η_e)	avg min t observed (μm)	avg max t observed (μm)	avg max/min ratio	min t observed (μm)	max t observed (μm)
Mg-12Li-2Nd/21Fe Casting	**0**	**6.64**	**28.82**	**4.64**	**4.90**	**78.21**
STDEV		1.99	7.66	1.63		
Mg-12Li-2Nd/21Fe Sheet	**1.89**	**2.75**	**17.09**	**6.69**	**1.24**	**25.00**
STDEV		0.81	4.18	2.31		
Mg-12Li-2Nd/21Fe Sheet	**3.67**	**0.40**	**5.43**	**15.03**	**0.23**	**13.33**
STDEV		0.19	3.32	8.02		
Mg-12Li-2Nd/21Fe Sheet	**3.97**	**0.76**	**6.64**	**10.98**	**0.30**	**12.02**
STDEV		0.39	2.88	8.63		
Mg-12Li-2Nd/21Fe Sheet	**5.55**	**0.17**	**2.78**	**23.81**	**0.05**	**4.17**
STDEV		0.15	1.21	17.46		
Mg-12Li-2Nd/21Fe Sheet	**6.5**	**0.23**	**3.20**	**16.12**	**0.06**	**12.69**
STDEV		0.14	2.80	18.05		
Mg-12Li-2Nd/21Fe Rod	**3.07**	**1.03**	**7.45**	**8.19**	**0.70**	**14.00**
STDEV		0.40	2.44	3.91		
Mg-12Li-2Nd/21Fe Rod	**4.29**	**0.56**	**8.33**	**16.45**	**0.38**	**17.29**
STDEV		0.24	3.46	8.20		
Mg-12Li-2Nd/21Fe Rod	**5.98**	**0.12**	**4.62**	**36.60**	**0.10**	**5.25**
STDEV		0.02	1.82	13.78		
Mg-4Li/27Fe Casting	**0**	**7.44**	**27.43**	**3.94**	**4.88**	**39.02**
STDEV		2.84	5.25	0.93		
Mg-4Li/27Fe Rod	**2.69**	**2.10**	**19.52**	**9.58**	**1.27**	**56.12**
STDEV		1.17	13.23	3.23		
Mg-4Li/27Fe Rod	**3.92**	**0.52**	**15.75**	**33.31**	**0.30**	**23.00**
STDEV		0.17	4.51	14.29		

Table C4. Stereological Measurements for the Mg-12Li-2Nd/21Fe Casting ($\eta = 0$)

pic#	scope	mag	orient	vol fr (ex)	vol fr (th)	N (cm^{-1})	λ (ex) (μm)	λ (th) (μm)	t (ex) (μm)	t (th) (μm)	t (ruler) (μm)
2035	SEM	450	L	0.23	0.21	0.43	40.29	41.19	11.85	10.95	13.60
2241	SEM	95.9	N	0.30	0.21	1.50	48.66	54.92	20.86	14.60	
2242	SEM	200	N	0.26	0.21	0.68	54.74	58.21	18.95	15.47	
2244	SEM	404	N	0.23	0.21	0.39	48.60	49.77	14.40	13.23	11.84
2246	SEM	95.9	N	0.34	0.21	1.07	63.96	76.89	33.37	20.44	
2247	SEM	200	N	0.19	0.21	0.64	63.33	61.44	14.44	16.33	15.08
2249	SEM	97.6	L	0.30	0.21	1.54	46.70	52.71	20.02	14.01	
2250	SEM	204	L	0.20	0.21	0.82	47.74	47.14	11.94	12.53	
2257	SEM	200	T	0.37	0.21	0.93	33.85	42.54	20.00	11.31	
2258	SEM	95.9	T	0.34	0.21	1.68	40.82	49.08	21.30	13.05	
2259	SEM	200	T	0.26	0.21	0.75	49.52	52.67	17.14	14.00	
2261	SEM	200	T	0.23	0.21	0.82	46.96	48.09	13.91	12.78	
2264	SEM	200	T	0.20	0.21	0.93	43.08	42.54	10.77	11.31	
2265	SEM	400	T	0.27	0.21	0.39	46.36	50.27	17.27	13.36	10.87
2031	SEM	100	N	0.26	0.21	1.12	65.88	70.46	23.31	18.73	
2034	SEM	100	L	0.32	0.21	1.70	40.18	46.55	18.75	12.38	
2035	SEM	300	L	0.22	0.21	0.55	47.92	48.28	13.19	12.83	
2036	SEM	100	T	0.22	0.21	1.64	47.92	48.28	13.19	12.83	
2241	SEM	95.9	N	0.33	0.21	1.54	45.59	53.64	22.31	14.26	
2242	SEM	200	N	0.21	0.21	0.75	52.38	52.67	14.29	14.00	
2244	SEM	404	N	0.20	0.21	0.36	55.45	54.75	13.86	14.55	
2246	SEM	95.9	N	0.26	0.21	0.93	83.42	88.71	28.88	23.58	
2247	SEM	200	N	0.20	0.21	0.64	62.22	61.44	15.56	16.33	
2249	SEM	97.6	L	0.27	0.21	1.79	41.80	45.33	15.57	12.05	
2250	SEM	204	L	0.19	0.21	0.79	50.80	49.29	11.59	13.10	
2257	SEM	200	T	0.36	0.21	0.71	45.00	55.30	25.00	14.70	
2258	SEM	95.9	T	0.31	0.21	1.54	46.56	53.64	21.34	14.26	
2259	SEM	200	T	0.24	0.21	0.96	39.26	40.96	12.59	10.89	
2261	SEM	200	T	0.29	0.21	0.96	37.04	40.96	14.81	10.89	
2264	SEM	200	T	0.30	0.21	1.11	31.61	35.68	13.55	9.48	
2265	SEM	404	T	0.24	0.21	0.46	40.37	42.12	12.95	11.20	
2267	SEM	200	T	0.33	0.21	0.89	37.60	44.24	18.40	11.76	

Table C5. Average Stereological Measurements for the Mg-12Li-2Nd/21Fe Casting ($\eta = 0$)

	vol fr (ex)	vol fr (th)	N (cm^{-1})	λ (ex) (μm)	λ (th) (μm)	t (ex) (μm)	t (th) (μm)	t (ruler) (μm)
AVERAGE ALL	**0.26**	**0.21**	**0.97**	**48.65**	**52.11**	**17.32**	**13.85**	**12.85**
STDEV ALL	0.05	0	0.44	10.59	10.99	5.36	2.92	1.87
AVERAGE ALL N	**0.25**	**0.21**	**0.87**	**58.57**	**62.08**	**20.02**	**16.50**	**13.46**
STDEV ALL N	0.05	0	0.40	10.79	11.96	6.54	3.18	2.29
AVERAGE ALL L	**0.25**	**0.21**	**1.09**	**45.06**	**47.21**	**14.70**	**12.55**	**13.60**
STDEV ALL L	0.05	0	0.57	4.25	3.56	3.49	0.95	
AVERAGE ALL T	**0.28**	**0.21**	**0.98**	**41.85**	**46.17**	**16.59**	**12.27**	**10.87**
STDEV ALL T	0.05	0	0.39	5.52	5.72	4.16	1.52	
AVERAGE ALL L+T	**0.27**	**0.21**	**1.02**	**42.92**	**46.52**	**15.96**	**12.37**	**12.24**
STDEV ALL L+T	0.06	0	0.45	5.25	5.03	3.97	1.34	1.93

Table C6. Minimum and Maximum Fe Fibers in the Mg-12Li-2Nd/21Fe Casting ($\eta = 0$)

pic#	scope	mag	orient	min t (μm)	max t (μm)	max/min ratio
2035	SEM	450	L	4.40	32.20	7.32
2241	SEM	95.9	N			
2242	SEM	200	N			
2244	SEM	404	N	5.57	23.51	4.22
2246	SEM	95.9	N			
2247	SEM	200	N	6.25	31.25	5.00
2249	SEM	97.6	L			
2250	SEM	204	L			
2257	SEM	200	T			
2258	SEM	95.9	T			
2259	SEM	200	T			
2261	SEM	200	T			
2264	SEM	200	T			
2265	SEM	400	T	5.00	20.63	4.13
2031	SEM	100	N	10.00	40.00	4.00
2034	SEM	100	L	8.00	32.00	4.00
2035	SEM	300	L	5.00	33.33	6.67
2036	SEM	100	T	10.00	45.00	4.50
2241	SEM	95.9	N	8.34	41.71	5.00
2242	SEM	200	N	9.00	37.50	4.17
2244	SEM	404	N	7.43	23.51	3.17
2246	SEM	95.9	N	5.21	78.21	15.00
2247	SEM	200	N	10.00	32.50	3.25
2249	SEM	97.6	L	7.17	25.61	3.57
2250	SEM	204	L	4.90	19.61	4.00
2257	SEM	200	T	7.50	27.50	3.67
2258	SEM	95.9	T	7.30	36.50	5.00
2259	SEM	200	T	10.00	25.00	2.50
2261	SEM	200	T	5.00	22.50	4.50
2264	SEM	200	T	5.00	37.50	7.50
2265	SEM	404	T	8.66	18.56	2.14
2267	SEM	200	T	5.00	27.50	5.50
AVERAGE ALL				**7.13**	**32.58**	**4.92**
STDEV ALL				1.98	12.94	2.69
AVERAGE ALL N				**7.73**	**38.52**	**5.48**
STDEV ALL N				1.91	17.43	3.91
AVERAGE ALL L				**5.89**	**28.55**	**5.11**
STDEV ALL L				1.59	5.85	1.74
AVERAGE ALL T				**7.05**	**28.97**	**4.38**
STDEV ALL T				2.15	8.85	1.60
AVERAGE ALL L+T				**6.64**	**28.82**	**4.64**
STDEV ALL L+T				1.99	7.66	1.63

Table C7. Stereological Measurements for Mg-12Li-2Nd/21Fe Sheet (η_e = 1.89)

pic#	scope	mag	orient	vol fr (ex)	vol fr (th)	N (cm^{-1})	λ (ex) (μm)	λ (th) (μm)	t (ex) (μm)	t (th) (μm)	t (ruler) (μm)
2224	SEM	404	T	0.43	0.21	1.61	8.80	12.17	6.60	3.23	
2226	SEM	404	T	0.41	0.21	1.29	11.28	15.21	7.98	4.04	
2228	SEM	404	T	0.36	0.21	0.96	16.50	20.28	9.17	5.39	
2230	SEM	404	T	0.37	0.21	1.50	10.37	13.04	6.13	3.47	
2232	SEM	404	T	0.31	0.21	1.14	14.85	17.11	6.81	4.55	
2235	SEM	404	T	0.26	0.21	1.43	12.87	13.69	4.46	3.64	
0000	SEM	370	T	0.26	0.21	1.42	14.02	14.99	4.96	3.99	
0002	SEM	500	T	0.32	0.21	1.00	13.64	15.80	6.36	4.20	
2215	SEM	200	L	0.39	0.21	2.07	14.83	19.07	9.31	5.07	
2216	SEM	404	L	0.33	0.21	1.43	11.63	13.69	5.69	3.64	
2217	SEM	200	L	0.36	0.21	1.93	16.67	20.48	9.26	5.44	
2218	SEM	404	L	0.26	0.21	1.36	13.55	14.41	4.69	3.83	
2219	SEM	200	L	0.44	0.21	2.25	12.38	17.56	9.84	4.67	
2220	SEM	404	L	0.29	0.21	1.04	17.07	18.88	6.83	5.02	
2221	SEM	200	L	0.27	0.21	3.04	12.00	13.01	4.47	3.46	
2222	SEM	404	L	0.27	0.21	1.54	11.74	12.73	4.37	3.38	
2223	SEM	200	T	0.36	0.21	2.07	15.52	19.07	8.62	5.07	
2224	SEM	404	T	0.30	0.21	1.21	14.27	16.10	6.12	4.28	
2225	SEM	200	T	0.40	0.21	2.54	11.83	15.58	7.89	4.14	
2226	SEM	404	T	0.40	0.21	1.04	14.34	18.88	9.56	5.02	
2227	SEM	200	T	0.20	0.21	1.54	26.05	25.72	6.51	6.84	
2228	SEM	404	T	0.31	0.21	0.93	18.28	21.06	8.38	5.60	
2229	SEM	200	T	0.24	0.21	2.61	14.52	15.15	4.66	4.03	
2230	SEM	404	T	0.31	0.21	1.54	11.05	12.73	5.07	3.38	
2231	SEM	200	T	0.33	0.21	2.39	14.03	16.51	6.87	4.39	
2232	SEM	404	T	0.26	0.21	1.00	18.39	19.55	6.36	5.20	
2234	SEM	200	T	0.34	0.21	1.96	16.73	20.11	8.73	5.35	
2235	SEM	404	T	0.21	0.21	1.39	13.96	14.04	3.81	3.73	

Table C8. Average Stereological Measurements for Mg-12Li-2Nd/21Fe Sheet (η_e = 1.89)

	vol fr (ex)	vol fr (th)	N (cm^{-1})	λ (ex) (μm)	λ (th) (μm)	t (ex) (μm)	t (th) (μm)	t (ruler) (μm)
AVERAGE ALL	**0.32**	**0.21**	**1.61**	**14.33**	**16.66**	**6.77**	**4.43**	
STDEV ALL	0.06	0.00	0.56	3.30	3.27	1.83	0.87	
AVERAGE ALL L	**0.33**	**0.21**	**1.83**	**13.73**	**16.23**	**6.81**	**4.31**	
STDEV ALL L	0.07	0.00	0.63	2.21	3.10	2.35	0.82	
AVERAGE ALL T	**0.32**	**0.21**	**1.53**	**14.56**	**16.84**	**6.75**	**4.48**	
STDEV ALL T	0.07	0.00	0.53	3.67	3.39	1.66	0.90	

Table C9. Minimum and Maximum Fe Fibers in Mg-12Li-2Nd/21Fe Sheet (η_e = 1.89)

pic#	scope	mag	orient	min t (μm)	max t (μm)	max/min ratio
2224	SEM	404	T			
2226	SEM	404	T			
2228	SEM	404	T			
2230	SEM	404	T			
2232	SEM	404	T			
2235	SEM	404	T			
0000	SEM	370	T	2.70	16.22	6.00
0002	SEM	500	T	2.00	20.00	10.00
2215	SEM	200	L	2.50	20.00	8.00
2216	SEM	404	L	3.71	14.85	4.00
2217	SEM	200	L	3.00	25.00	8.33
2218	SEM	404	L	3.71	9.90	2.67
2219	SEM	200	L	3.50	22.50	6.43
2220	SEM	404	L	3.71	22.28	6.00
2221	SEM	200	L	2.50	20.00	8.00
2222	SEM	404	L	2.48	14.85	6.00
2223	SEM	200	T	2.50	17.50	7.00
2224	SEM	404	T	2.48	16.09	6.50
2225	SEM	200	T	3.00	20.00	6.67
2226	SEM	404	T	2.48	19.80	8.00
2227	SEM	200	T	5.00	17.50	3.50
2228	SEM	404	T	2.48	9.90	4.00
2229	SEM	200	T	2.50	20.00	8.00
2230	SEM	404	T	1.24	14.85	12.00
2231	SEM	200	T	2.50	17.50	7.00
2232	SEM	404	T	2.48	9.90	4.00
2234	SEM	200	T	1.50	15.00	10.00
2235	SEM	404	T	2.48	12.38	5.00
AVERAGE ALL				**2.75**	**17.09**	**6.69**
STDEV ALL				0.81	4.18	2.31
AVERAGE ALL L				**3.14**	**18.67**	**6.18**
STDEV ALL L				0.58	5.03	2.02
AVERAGE ALL T				**2.52**	**16.19**	**6.98**
STDEV ALL T				0.85	3.49	2.49

Table C10. Stereological Measurements for Mg-12Li-2Nd/21Fe Sheet ($\eta_e = 3.67$)

pic#	scope	mag	orient	vol fr (ex)	vol fr (th)	N (cm^{-1})	λ (ex) (μm)	λ (th) (μm)	t (ex) (μm)	t (th) (μm)	t (ruler) (μm)
0017	TEM	7400	T	0.41	0.21	0.23	3.50	4.65	2.39	1.24	1.29
J003	TEM	4400	T	0.35	0.21	0.79	1.88	2.29	1.01	0.61	
J008	TEM	3000	T	0.28	0.21	0.68	3.54	3.88	1.37	1.03	
J012	TEM	3900	T	0.22	0.21	0.50	3.99	4.05	1.14	1.08	
J013	TEM	3900	T	0.16	0.21	0.50	4.30	4.05	0.82	1.08	
J015	TEM	1700	T	0.34	0.21	0.39	9.89	11.83	5.08	3.14	
J017	TEM	3000	T	0.32	0.21	0.46	4.90	5.67	2.28	1.51	
J018	TEM	3000	T	0.37	0.21	0.86	2.47	3.07	1.42	0.82	
J019	TEM	3000	T	0.48	0.21	0.39	4.44	6.70	4.04	1.78	
J020	TEM	3000	T	0.16	0.21	0.57	4.91	4.61	0.93	1.23	
J022	TEM	3000	T	0.21	0.21	0.50	5.29	5.27	1.38	1.40	
J023	TEM	3000	T	0.29	0.21	0.39	6.06	6.70	2.42	1.78	

Table C11. Average Stereological Measurements for Mg-12Li-2Nd/21Fe Sheet ($\eta_e = 3.67$)

	vol fr (ex)	vol fr (th)	N (cm^{-1})	λ (ex) (μm)	λ (th) (μm)	t (ex) (μm)	t (th) (μm)	t (ruler) (μm)
AVERAGE ALL	**0.30**	**0.21**	**0.52**	**4.60**	**5.23**	**2.02**	**1.39**	**1.29**
STDEV ALL	0.10	0.00	0.18	2.03	2.46	1.33	0.65	

Table C12. Minimum and Maximum Fe Fibers in Mg-12Li-2Nd/21Fe Sheet ($\eta_e = 3.67$)

pic#	scope	mag	orient	min t (μm)	max t (μm)	max/min ratio
0017	TEM	7400	T	0.26	4.80	18.46
J003	TEM	4400	T	0.23	3.11	13.70
J008	TEM	3000	T	0.33	7.33	22.00
J012	TEM	3900	T	0.51	2.44	4.75
J013	TEM	3900	T	0.51	1.67	3.25
J015	TEM	1700	T	0.88	8.53	9.67
J017	TEM	3000	T	0.33	7.67	23.00
J018	TEM	3000	T	0.17	4.00	24.00
J019	TEM	3000	T	0.50	13.33	26.67
J020	TEM	3000	T	0.33	5.83	17.50
J022	TEM	3000	T	0.43	3.00	6.92
J023	TEM	3000	T	0.33	3.50	10.50
AVERAGE ALL				**0.40**	**5.43**	**15.03**
STDEV ALL				0.19	3.32	8.02

Table C13. Stereological Measurements for Mg-12Li-2Nd/21Fe Sheet (η_e = 3.97)

pic#	scope	mag	orient	vol fr (ex)	vol fr (th)	N (cm^{-1})	λ (ex) (μm)	λ (th) (μm)	t (ex) (μm)	t (th) (μm)	t (ruler) (μm)
2039	SEM	500	L	0.20	0.21	3.30	4.82	4.78	1.24	1.27	2.76
2040	SEM	2000	L	0.38	0.21	1.00	3.13	3.95	1.88	1.05	1.40
2189	SEM	984	T	0.41	0.21	1.79	3.33	4.50	2.36	1.20	
2190	SEM	501	T	0.44	0.21	2.61	4.27	6.05	3.39	1.61	
2191	SEM	984	T	0.34	0.21	1.54	4.35	5.23	2.27	1.39	
2192	SEM	501	T	0.39	0.21	2.68	4.58	5.89	2.87	1.56	
2193	SEM	984	T	0.46	0.21	1.79	3.09	4.50	2.60	1.20	
2194	SEM	501	T	0.46	0.21	3.71	2.92	4.25	2.46	1.13	
2195	SEM	984	T	0.37	0.21	2.00	3.19	4.01	1.89	1.07	
2197	SEM	984	T	0.36	0.21	1.54	4.25	5.23	2.36	1.39	
2200	SEM	984	T	0.33	0.21	1.89	3.60	4.24	1.76	1.13	
2202	SEM	984	T	0.30	0.21	1.79	3.98	4.50	1.71	1.20	
2204	SEM	984	T	0.40	0.21	1.54	3.97	5.23	2.65	1.39	
2206	SEM	4920	T	0.39	0.21	0.57	2.18	2.81	1.37	0.75	
2039	SEM	500	L	0.22	0.21	3.06	5.12	5.16	1.41	1.37	
2040	SEM	2000	L	0.36	0.21	0.94	3.39	4.20	1.94	1.12	
2043	SEM	500	T	0.23	0.21	2.73	5.67	5.79	1.67	1.54	
2044	SEM	2000	T	0.30	0.21	1.15	3.06	3.43	1.28	0.91	
2130	SEM	1010	T	0.31	0.21	1.36	5.00	5.76	2.29	1.53	
2133	SEM	1010	T	0.21	0.21	1.39	5.59	5.62	1.52	1.49	
2135	SEM	1010	T	0.23	0.21	1.21	6.29	6.44	1.86	1.71	
2187	SEM	998	L	0.29	0.21	1.39	5.14	5.68	2.06	1.51	
2189	SEM	984	T	0.36	0.21	1.39	4.69	5.76	2.61	1.53	
2191	SEM	984	T	0.27	0.21	1.29	5.76	6.24	2.15	1.66	
2193	SEM	984	T	0.36	0.21	1.61	4.07	5.00	2.26	1.33	
2195	SEM	984	T	0.31	0.21	1.75	3.98	4.59	1.83	1.22	
2197	SEM	984	T	0.36	0.21	1.39	4.69	5.76	2.61	1.53	
2200	SEM	984	T	0.39	0.21	1.71	3.64	4.68	2.29	1.24	
2202	SEM	984	T	0.30	0.21	1.86	3.83	4.32	1.64	1.15	
2204	SEM	984	T	0.39	0.21	1.61	3.88	5.00	2.44	1.33	
2207	SEM	4920	T	0.24	0.21	0.54	2.87	3.00	0.92	0.80	

Table C14. Average Stereological Measurements for Mg-12Li-2Nd/21Fe Sheet (η_e = 3.97)

	vol fr (ex)	vol fr (th)	N (cm^{-1})	λ (ex) (μm)	λ (th) (μm)	t (ex) (μm)	t (th) (μm)	t (ruler) (μm)
AVERAGE ALL	**0.33**	**0.21**	**1.75**	**4.14**	**4.89**	**2.05**	**1.30**	**2.08**
STDEV ALL	0.07	0.00	0.74	0.98	0.92	0.54	0.24	0.96
AVERAGE ALL L	**0.29**	**0.21**	**2.08**	**4.11**	**4.53**	**1.61**	**1.20**	**2.08**
STDEV ALL L	0.09	0.00	1.28	1.00	0.55	0.34	0.15	0.96
AVERAGE ALL T	**0.34**	**0.21**	**1.71**	**4.11**	**4.92**	**2.12**	**1.31**	
STDEV ALL T	0.07	0.00	0.66	1.00	0.96	0.55	0.26	

Table C15. Minimum and Maximum Fe Fibers in Mg-12Li-2Nd/21Fe Sheet ($\eta_e = 3.97$)

pic#	scope	mag	orient	min t (μm)	max t (μm)	max/min ratio
2039	SEM	500	L	0.70	13.10	18.71
2040	SEM	2000	L	0.17	3.67	21.59
2189	SEM	984	T			
2190	SEM	501	T			
2191	SEM	984	T			
2192	SEM	501	T			
2193	SEM	984	T			
2194	SEM	501	T			
2195	SEM	984	T			
2197	SEM	984	T			
2200	SEM	984	T			
2202	SEM	984	T			
2204	SEM	984	T			
2206	SEM	4920	T			
2039	SEM	500	L	2.00	8.00	4.00
2040	SEM	2000	L	1.00	3.75	3.75
2043	SEM	500	T	0.60	8.00	13.33
2044	SEM	2000	T	0.50	7.50	15.00
2130	SEM	1010	T	0.99	3.96	4.00
2133	SEM	1010	T	0.50	5.45	11.00
2135	SEM	1010	T	0.50	5.45	11.00
2187	SEM	998	L	0.30	12.02	40.00
2189	SEM	984	T	0.71	6.10	8.57
2191	SEM	984	T	1.02	6.10	6.00
2193	SEM	984	T	0.71	5.08	7.14
2195	SEM	984	T	0.81	7.11	8.75
2197	SEM	984	T	1.02	8.64	8.50
2200	SEM	984	T	0.81	6.10	7.50
2202	SEM	984	T	0.71	6.10	8.57
2204	SEM	984	T	1.02	9.15	9.00
2207	SEM	4920	T	0.41	0.91	2.25
AVERAGE ALL				**0.76**	**6.64**	**10.98**
STDEV ALL				0.39	2.88	8.63
AVERAGE ALL L				**0.97**	**7.13**	**12.01**
STDEV ALL L				0.77	4.46	9.47
AVERAGE ALL T				**0.74**	**6.12**	**8.62**
STDEV ALL T				0.22	2.07	3.36

Table C16. Stereological Measurements for Mg-12Li-2Nd/21Fe Sheet ($\eta_e = 5.55$)

pic#	scope	mag	orient	vol fr (ex)	vol fr (th)	N (cm^{-1})	λ (ex) (μm)	λ (th) (μm)	t (ex) (μm)	t (th) (μm)	t (ruler) (μm)
0003	TEM	9700	T	0.29	0.21	0.60	1.22	1.36	0.50	0.36	0.34
0003	TEM	3900	T	0.30	0.21	1.86	0.96	1.09	0.42	0.29	
0017	TEM	3000	T	0.21	0.21	0.86	3.06	3.07	0.83	0.82	

Table C17. Average Stereological Measurements for Mg-12Li-2Nd/21Fe Sheet ($\eta_e = 5.55$)

	vol fr (ex)	vol fr (th)	N (cm^{-1})	λ (ex) (μm)	λ (th) (μm)	t (ex) (μm)	t (th) (μm)	t (ruler) (μm)
AVERAGE ALL	**0.27**	**0.21**	**1.10**	**1.75**	**1.84**	**0.58**	**0.49**	**0.34**
STDEV ALL	0.05	0.00	0.66	1.14	1.07	0.22	0.29	

Table C18. Minimum and Maximum Fe Fibers in Mg-12Li-2Nd/21Fe Sheet ($\eta_e = 5.55$)

pic#	scope	mag	orient	min t (μm)	max t (μm)	max/min ratio
0003	TEM	9700	T	0.05	2.24	43.92
0003	TEM	3900	T	0.13	1.92	15.00
0017	TEM	3000	T	0.33	4.17	12.50
AVERAGE ALL				**0.17**	**2.78**	**23.81**
STDEV ALL				0.15	1.21	17.46

Table C19. Stereological Measurements for Mg-12Li-2Nd/21Fe Sheet ($\eta_e = 6.5$)

pic#	scope	mag	orient	vol fr (ex)	vol fr (th)	N (cm^{-1})	λ (ex) (μm)	λ (th) (μm)	t (ex) (μm)	t (th) (μm)	t (ruler) (μm)
0001	SEM	3500	T		0.21	1.09	2.62	2.07		0.55	
0003	SEM	2500	T		0.21	2.18	1.83	1.45		0.39	
0004	SEM	10000	T		0.21	1.76	0.57	0.45		0.12	
0005	SEM	10000	T		0.21	1.39	0.72	0.57		0.15	
0035	SEM	3000	T	0.38	0.21	1.24	1.68	2.12	1.01	0.56	
0038	SEM	2000	T	0.28	0.21	1.82	1.97	2.17	0.78	0.58	
0042	SEM	5000	T		0.21	2.00	1.00	0.79		0.21	
0081	SEM	5000	T		0.21	1.00	2.00	1.58		0.42	
2005	SEM	1000	L		0.21	4.39	2.28	1.80		0.48	0.98
2011	SEM	10000	L	0.33	0.21	0.91	0.74	0.87	0.36	0.23	0.28
2167	SEM	2070	L	0.34	0.21	2.11	1.51	1.81	0.79	0.48	
J601-	TEM	2110	T	0.34	0.21	2.23	1.39	1.68	0.73	0.45	
J507-	TEM	5610	T	0.31	0.21	0.65	1.90	2.17	0.84	0.58	
2167	SEM	2070	L	0.26	0.21	1.93	1.86	1.98	0.64	0.53	
2173	SEM	2070	T	0.27	0.21	1.32	2.66	2.89	0.99	0.77	
2174	SEM	2070	T	0.31	0.21	1.25	2.65	3.05	1.21	0.81	
2176	SEM	2070	T	0.33	0.21	1.86	1.75	2.05	0.85	0.55	
2177	SEM	1970	T	0.39	0.21	1.11	2.82	3.62	1.77	0.96	
2178	SEM	2070	T	0.37	0.21	1.43	2.13	2.67	1.26	0.71	
2179	SEM	2070	T	0.36	0.21	1.64	1.89	2.32	1.05	0.62	
2180	SEM	2070	T	0.37	0.21	1.71	1.77	2.23	1.05	0.59	
0035	SEM	3000	T	0.31	0.21	1.24	1.86	2.12	0.82	0.56	
0038	SEM	2000	T	0.20	0.21	1.70	2.34	2.33	0.60	0.62	
0042	SEM	5000	T	0.23	0.21	1.70	0.91	0.93	0.27	0.25	
0001	SEM	3500	T	0.33	0.21	0.97	1.98	2.33	0.97	0.62	
0003	SEM	2500	T	0.26	0.21	1.94	1.53	1.63	0.53	0.43	
0005	SEM	10000	T	0.27	0.21	1.42	0.51	0.55	0.19	0.15	
0006	SEM	5000	T	0.19	0.21	1.82	0.89	0.87	0.21	0.23	
0007	SEM	19900	T	0.16	0.21	0.76	0.56	0.52	0.11	0.14	
0081	SEM	5000	T	0.23	0.21	0.97	1.59	1.63	0.47	0.43	
0003	SEM	2500	T	0.27	0.21	0.97	3.00	3.26	1.13	0.87	
2007	SEM	20000	L	0.31	0.21	0.48	0.71	0.81	0.32	0.22	
2008	SEM	10000	L	0.17	0.21	0.79	1.05	1.00	0.22	0.27	
2011	SEM	10000	L	0.34	0.21	0.97	0.68	0.81	0.35	0.22	
2012	SEM	40000	L	0.36	0.21	0.48	0.33	0.41	0.19	0.11	
2014	SEM	10000	L	0.47	0.21	0.61	0.88	1.30	0.77	0.35	
2016	SEM	20000	L	0.33	0.21	0.42	0.79	0.93	0.39	0.25	
2022	SEM	10000	T	0.26	0.21	0.61	1.22	1.30	0.43	0.35	
2027	SEM	10000	T	0.26	0.21	0.73	1.02	1.09	0.36	0.29	

Table C20. Average Stereological Measurements for Mg-12Li-2Nd/21Fe Sheet ($\eta_e = 6.5$)

	vol fr (ex)	vol fr (th)	N (cm^{-1})	λ (ex) (μm)	λ (th) (μm)	t (ex) (μm)	t (th) (μm)	t (ruler) (μm)
AVERAGE ALL	**0.30**	**0.21**	**1.37**	**1.53**	**1.65**	**0.68**	**0.44**	**0.63**
STDEV ALL	0.07	0.00	0.72	0.73	0.83	0.39	0.22	0.49
AVERAGE ALL L	**0.32**	**0.21**	**1.33**	**1.18**	**1.30**	**0.51**	**0.35**	**0.63**
STDEV ALL L	0.07	0.00	1.17	0.60	0.57	0.25	0.15	0.49
AVERAGE ALL T	**0.29**	**0.21**	**1.40**	**1.68**	**1.81**	**0.77**	**0.48**	
STDEV ALL T	0.06	0.00	0.46	0.71	0.86	0.41	0.23	

Table C21. Minimum and Maximum Fe Fibers in Mg-12Li-2Nd/21Fe Sheet ($\eta_e = 6.5$)

pic#	scope	mag	orient	min t (μm)	max t (μm)	max/min ratio
0001	SEM	3500	T			
0003	SEM	2500	T			
0004	SEM	10000	T			
0005	SEM	10000	T			
0035	SEM	3000	T			
0038	SEM	2000	T			
0042	SEM	5000	T			
0081	SEM	5000	T			
2005	SEM	1000	L	0.33	6.00	18.18
2011	SEM	10000	L	0.07	0.80	11.94
2167	SEM	2070	L			
J601-	TEM	2110	T	0.24	6.40	27.00
J507-	TEM	5610	T	0.09	9.27	104.00
2167	SEM	2070	L	0.19	3.38	17.50
2173	SEM	2070	T	0.48	3.38	7.00
2174	SEM	2070	T	0.29	3.86	13.33
2176	SEM	2070	T	0.34	3.86	11.43
2177	SEM	1970	T	0.51	12.69	25.00
2178	SEM	2070	T	0.48	6.04	12.50
2179	SEM	2070	T	0.48	4.35	9.00
2180	SEM	2070	T	0.24	3.38	14.00
0035	SEM	3000	T	0.17	2.00	12.00
0038	SEM	2000	T	0.35	3.50	10.00
0042	SEM	5000	T	0.10	1.00	10.00
0001	SEM	3500	T	0.17	2.14	12.50
0003	SEM	2500	T	0.40	3.00	7.50
0005	SEM	10000	T	0.10	0.80	8.00
0006	SEM	5000	T	0.06	1.80	30.00
0007	SEM	19900	T	0.07	0.28	4.23

Table C21. (continued)

pic#	scope	mag	orient	min t (μm)	max t (μm)	max/min ratio
0081	SEM	5000	T	0.20	4.00	20.00
0003	SEM	2500	T	0.20	5.20	26.00
2007	SEM	20000	L	0.08	1.15	15.33
2008	SEM	10000	L	0.08	1.60	20.00
2011	SEM	10000	L	0.15	0.60	4.00
2012	SEM	40000	L	0.06	0.43	6.80
2014	SEM	10000	L	0.30	1.70	5.67
2016	SEM	20000	L	0.09	0.85	9.44
2022	SEM	10000	T	0.25	0.80	3.20
2027	SEM	10000	T	0.20	1.60	8.00
AVERAGE ALL				**0.23**	**3.20**	**16.12**
STDEV ALL				0.14	2.80	18.05
AVERAGE ALL L				**0.15**	**2.92**	**21.81**
STDEV ALL L				0.10	2.98	28.13
AVERAGE ALL T				**0.26**	**3.78**	**17.84**
STDEV ALL T				0.15	2.98	21.17

Table C22. Stereological Measurements for Mg-12Li-2Nd/21Fe Rod ($\eta = 3.07$)

pic#	scope	mag	orient	vol fr (ex)	vol fr (th)	N (cm^{-1})	λ (ex) (μm)	λ (th) (μm)	t (ex) (μm)	t (th) (μm)	t (ruler) (μm)
0010	SEM	500	T	0.31	0.21	2.12	6.54	7.45	2.89	1.98	
0011	SEM	1000	T	0.36	0.21	1.48	4.29	5.32	2.45	1.41	
0012	SEM	1000	T	0.22	0.21	0.85	9.24	9.31	2.54	2.48	
G003	TEM	2110	T	0.35	0.21	0.57	5.40	6.55	2.90	1.74	
G015	TEM	2110	T	0.41	0.21	0.54	5.20	6.99	3.65	1.86	
G018	TEM	2110	T	0.32	0.21	0.39	8.23	9.53	3.83	2.53	
G019	TEM	2110	T	0.17	0.21	0.25	15.65	14.98	3.31	3.98	
G020	TEM	2110	T	0.33	0.21	0.55	5.79	6.86	2.90	1.82	
G021	TEM	2110	T	0.28	0.21	0.45	7.53	8.24	2.90	2.19	
G022	TEM	2110	T	0.31	0.21	0.36	9.05	10.30	3.98	2.74	
G023	TEM	2110	T	0.31	0.21	0.52	6.39	7.27	2.81	1.93	
G024	TEM	2110	T	0.25	0.21	0.30	11.73	12.36	3.91	3.28	
G025	TEM	2110	T	0.32	0.21	0.48	6.65	7.72	3.12	2.05	
G026	TEM	2110	T	0.38	0.21	0.48	6.11	7.72	3.67	2.05	
G028	TEM	2110	T	0.43	0.21	0.48	5.57	7.72	4.21	2.05	
G029	TEM	2110	T	0.43	0.21	0.52	5.24	7.27	3.96	1.93	
G031	TEM	2110	T	0.42	0.21	0.55	5.07	6.86	3.62	1.82	
G032	TEM	2110	T	0.49	0.21	0.58	4.23	6.50	4.00	1.73	
G033	TEM	2110	T	0.18	0.21	0.24	16.02	15.44	3.53	4.11	
G034	TEM	2110	T	0.35	0.21	0.39	7.85	9.50	4.18	2.53	

Table C22. (continued)

pic#	scope	mag	orient	vol fr (ex)	vol fr (th)	N (cm^{-1})	λ (ex) (μm)	λ (th) (μm)	t (ex) (μm)	t (th) (μm)	t (ruler) (μm)
G037	TEM	2110	T	0.26	0.21	0.36	9.59	10.30	3.44	2.74	
G038	TEM	2110	T	0.38	0.21	0.42	6.98	8.83	4.19	2.35	
G040	TEM	2110	T	0.39	0.21	0.52	5.62	7.27	3.58	1.93	
G042	TEM	2110	T	0.39	0.21	0.52	5.62	7.27	3.58	1.93	
G045	TEM	2110	T	0.36	0.21	0.42	7.14	8.83	4.03	2.35	
G046	TEM	2110	T	0.28	0.21	0.42	8.07	8.83	3.10	2.35	
0010	SEM	500	T	0.31	0.21	2.03	6.83	7.78	3.02	2.07	
0011	SEM	1000	T	0.32	0.21	1.39	4.89	5.67	2.28	1.51	
0012	SEM	1000	T	0.28	0.21	1.03	6.95	7.67	2.76	2.04	
G001	TEM	3000	T	0.29	0.21	0.36	6.67	7.37	2.67	1.96	
G002	TEM	3000	T	0.50	0.21	0.39	4.24	6.70	4.24	1.78	
G003	TEM	2110	T	0.32	0.21	0.54	6.04	6.99	2.81	1.86	
G015	TEM	2110	T	0.27	0.21	0.54	6.46	6.99	2.39	1.86	
G018	TEM	2110	T	0.32	0.21	0.36	9.06	10.48	4.21	2.79	
G019	TEM	2110	T	0.22	0.21	0.29	12.90	13.10	3.69	3.48	
G021	TEM	2110	T	0.33	0.21	0.61	5.20	6.17	2.60	1.64	
G022	TEM	2110	T	0.24	0.21	0.46	7.78	8.06	2.43	2.14	
G023	TEM	2110	T	0.32	0.21	0.50	6.47	7.49	3.01	1.99	
G026	TEM	2110	T	0.33	0.21	0.57	5.53	6.55	2.76	1.74	
G028	TEM	2110	T	0.44	0.21	0.46	5.67	8.06	4.54	2.14	
G029	TEM	2110	T	0.43	0.21	0.64	4.21	5.82	3.16	1.55	
G031	TEM	2110	T	0.49	0.21	0.57	4.21	6.55	4.08	1.74	
G032	TEM	2110	T	0.49	0.21	0.46	5.18	8.06	5.02	2.14	
G034	TEM	2110	T	0.43	0.21	0.43	6.32	8.74	4.74	2.32	
G037	TEM	2110	T	0.22	0.21	0.54	6.88	6.99	1.97	1.86	
G038	TEM	2110	T	0.41	0.21	0.46	6.00	8.06	4.21	2.14	
G040	TEM	2110	T	0.35	0.21	0.54	5.76	6.99	3.09	1.86	
G042	TEM	2110	T	0.43	0.21	0.46	5.83	8.06	4.37	2.14	
G043	TEM	2110	T	0.44	0.21	0.46	5.67	8.06	4.54	2.14	
G047	TEM	2110	T	0.33	0.21	0.46	6.81	8.06	3.40	2.14	

Table C23. Average Stereological Measurements for Mg-12Li-2Nd/21Fe Rod ($\eta = 3.07$)

	vol fr (ex)	vol fr (th)	N (cm^{-1})	λ (ex) (μm)	λ (th) (μm)	t (ex) (μm)	t (th) (μm)	t (ruler) (μm)
AVERAGE ALL	**0.34**	**0.21**	**0.59**	**6.93**	**8.19**	**3.45**	**2.18**	
STDEV ALL	0.08	0.00	0.38	2.56	2.09	0.72	0.56	

Table C24. Minimum and Maximum Fe Fibers in Mg-12Li-2Nd/21Fe Rod (η = 3.07)

pic#	scope	mag	orient	min t (μm)	max t (μm)	max/min ratio
0010	SEM	500	T	0.80	9.00	11.25
0011	SEM	1000	T	0.70	14.00	20.00
0012	SEM	1000	T	1.00	10.00	10.00
G003	TEM	2110	T	0.71	13.27	18.67
G015	TEM	2110	T	0.95	8.06	8.50
G018	TEM	2110	T	0.71	8.06	11.33
G019	TEM	2110	T	0.71	3.55	5.00
G020	TEM	2110	T	0.71	6.40	9.00
G021	TEM	2110	T	0.71	5.69	8.00
G022	TEM	2110	T	0.71	4.74	6.67
G023	TEM	2110	T	0.95	8.06	8.50
G024	TEM	2110	T	0.71	5.69	8.00
G025	TEM	2110	T	0.71	7.11	10.00
G026	TEM	2110	T	0.95	8.53	9.00
G028	TEM	2110	T	0.95	9.48	10.00
G029	TEM	2110	T	0.71	6.64	9.33
G031	TEM	2110	T	0.95	8.53	9.00
G032	TEM	2110	T	0.59	7.58	12.80
G033	TEM	2110	T	0.95	4.74	5.00
G034	TEM	2110	T	0.71	6.64	9.33
G037	TEM	2110	T	0.71	6.16	8.67
G038	TEM	2110	T	0.71	7.11	10.00
G040	TEM	2110	T	0.71	8.06	11.33
G042	TEM	2110	T	0.71	7.58	10.67
G045	TEM	2110	T	0.71	7.11	10.00
G046	TEM	2110	T	1.18	8.53	7.20
0010	SEM	500	T	0.80	9.00	11.25
0011	SEM	1000	T	0.80	14.00	17.50
0012	SEM	1000	T	1.00	10.00	10.00
G001	TEM	3000	T	0.83	4.67	5.60
G002	TEM	3000	T	1.00	6.67	6.67
G003	TEM	2110	T	0.95	13.74	14.50
G015	TEM	2110	T	1.42	7.58	5.33
G018	TEM	2110	T	0.95	7.11	7.50
G019	TEM	2110	T	0.95	3.79	4.00
G021	TEM	2110	T	0.71	5.21	7.33
G022	TEM	2110	T	2.37	4.74	2.00
G023	TEM	2110	T	1.42	6.16	4.33
G026	TEM	2110	T	1.42	5.69	4.00

Table C24. (continued)

pic#	scope	mag	orient	min t (μm)	max t (μm)	max/min ratio
G028	TEM	2110	T	1.90	8.53	4.50
G029	TEM	2110	T	1.18	6.16	5.20
G031	TEM	2110	T	0.95	7.11	7.50
G032	TEM	2110	T	1.42	8.06	5.67
G034	TEM	2110	T	1.90	5.69	3.00
G037	TEM	2110	T	1.42	6.16	4.33
G038	TEM	2110	T	1.42	7.11	5.00
G040	TEM	2110	T	1.42	5.69	4.00
G042	TEM	2110	T	1.42	3.79	2.67
G043	TEM	2110	T	2.13	7.11	3.33
G047	TEM	2110	T	1.18	8.53	7.20
AVERAGE ALL				**1.03**	**7.45**	**8.19**
STDEV ALL				0.40	2.44	3.91

Table C25. Stereological Measurements for Mg-12Li-2Nd/21Fe Rod ($\eta = 4.29$)

pic#	scope	mag	orient	vol fr (ex)	vol fr (th)	N (cm^{-1})	λ (ex) (μm)	λ (th) (μm)	t (ex) (μm)	t (th) (μm)	t (ruler) (μm)
J106-	TEM	3900	T	0.40	0.21	0.58	2.63	3.49	1.79	0.93	
J121-	TEM	4400	T	0.39	0.21	0.50	2.77	3.59	1.77	0.95	
0047	SEM	1500	T		0.21	1.12	5.95	4.70		1.25	
0049	SEM	2000	T		0.21	1.00	5.00	3.95		1.05	
0089	SEM	1000	T		0.21	1.15	8.68	6.86		1.82	
0091	SEM	2500	T		0.21	0.79	5.08	4.01		1.07	
2311	SEM	781	L	0.26	0.21	1.50	6.34	6.74	2.19	1.79	
2313	SEM	781	L	0.26	0.21	1.79	5.33	5.66	1.84	1.51	
2316	SEM	781	L	0.33	0.21	1.79	4.81	5.66	2.36	1.51	
2321	SEM	781	T	0.33	0.21	1.68	5.12	6.03	2.51	1.60	
2322	SEM	1620	T	0.26	0.21	0.75	6.11	6.50	2.12	1.73	
2324	SEM	781	T	0.37	0.21	1.64	4.90	6.16	2.89	1.64	
2326	SEM	781	T	0.26	0.21	1.71	5.55	5.90	1.92	1.57	
2327	SEM	1620	T	0.29	0.21	0.93	4.75	5.25	1.90	1.40	
2329	SEM	781	T	0.44	0.21	2.39	2.98	4.23	2.37	1.12	
2330	SEM	1620	T	0.36	0.21	1.25	3.17	3.90	1.76	1.04	
2332	SEM	1620	T	0.34	0.21	1.07	3.79	4.55	1.98	1.21	
0047	SEM	1500	T	0.30	0.21	0.97	4.84	5.43	2.03	1.44	
0049	SEM	2000	T	0.22	0.21	0.82	4.79	4.83	1.32	1.28	
0050	SEM	1000	T	0.25	0.21	0.94	7.98	8.41	2.66	2.24	
0051	SEM	1000	T	0.23	0.21	1.36	5.67	5.79	1.67	1.54	
0089	SEM	1000	T	0.17	0.21	0.94	8.83	8.41	1.81	2.24	

Table C26. Average Stereological Measurements for Mg-12Li-2Nd/21Fe Rod ($\eta = 4.29$)

	vol fr (ex)	vol fr (th)	N (cm^{-1})	λ (ex) (μm)	λ (th) (μm)	t (ex) (μm)	t (th) (μm)	t (ruler) (μm)
AVERAGE ALL	**0.30**	**0.21**	**1.21**	**5.23**	**5.46**	**2.05**	**1.45**	
STDEV ALL	0.07	0.00	0.47	1.70	1.39	0.39	0.37	
AVERAGE ALL T	**0.31**	**0.21**	**1.14**	**5.19**	**5.37**	**2.03**	**1.43**	
STDEV ALL T	0.08	0.00	0.46	1.81	1.47	0.41	0.39	
AVERAGE ALL L	**0.28**	**0.21**	**1.69**	**5.49**	**6.02**	**2.13**	**1.60**	
STDEV ALL L	0.04	0.00	0.16	0.78	0.62	0.26	0.17	

Table C27. Minimum and Maximum Fe Fibers in Mg-12Li-2Nd/21Fe Rod ($\eta = 4.29$)

pic#	scope	mag	orient	min t (μm)	max t (μm)	max/min ratio
J106-	TEM	3900	T	0.26	7.18	28.00
J121-	TEM	4400	T	0.23	7.50	33.00
0047	SEM	1500	T			
0049	SEM	2000	T			
0089	SEM	1000	T			
0091	SEM	2500	T			
2311	SEM	781	L	0.64	11.52	18.00
2313	SEM	781	L	0.64	10.24	16.00
2316	SEM	781	L	1.28	17.29	13.50
2321	SEM	781	T	0.64	8.96	14.00
2322	SEM	1620	T	0.93	6.17	6.67
2324	SEM	781	T	0.38	12.80	33.33
2326	SEM	781	T	0.51	5.12	10.00
2327	SEM	1620	T	0.62	4.32	7.00
2329	SEM	781	T	0.51	8.32	16.25
2330	SEM	1620	T	0.43	6.17	14.29
2332	SEM	1620	T	0.43	5.25	12.14
0047	SEM	1500	T	0.67	8.00	12.00
0049	SEM	2000	T	0.50	4.50	9.00
0050	SEM	1000	T	0.50	7.00	14.00
0051	SEM	1000	T	0.50	13.00	26.00
0089	SEM	1000	T	0.50	6.50	13.00
AVERAGE ALL				**0.56**	**8.33**	**16.45**
STDEV ALL				0.24	3.46	8.20
AVERAGE ALL T				**0.51**	**7.39**	**16.58**
STDEV ALL T				0.17	2.62	8.99
AVERAGE ALL L				**0.85**	**13.02**	**15.83**
STDEV ALL L				0.37	3.75	2.25

Table C28. Stereological Measurements for Mg-12Li-2Nd/21Fe Rod (η = 5.98)

pic#	scope	mag	orient	vol fr (ex)	vol fr (th)	N (cm^{-1})	λ (ex) (μm)	λ (th) (μm)	t (ex) (μm)	t (th) (μm)	t (ruler) (μm)
D289-	TEM	4400	T	0.41	0.21	0.62	2.14	2.88		0.76	
D307-	TEM	3900	T	0.41	0.21	0.89	1.69	2.27		0.60	
D315-	TEM	3900	T	0.38	0.21	0.96	1.67	2.11		0.56	
0014	SEM	2000	T		0.21	1.21	4.13	3.26		0.87	
0015	SEM	5000	T		0.21	0.76	2.64	2.09		0.55	
0016	SEM	4940	T		0.21	0.70	2.90	2.29		0.61	
2419	SEM	3980	T		0.21	0.93	2.71	2.14		0.57	
0014	SEM	2000	T	0.22	0.21	1.33	2.94	2.96	0.81	0.79	
0015	SEM	5000	T	0.19	0.21	0.70	2.32	2.27	0.55	0.60	

Table C29. Average Stereological Measurements for Mg-12Li-2Nd/21Fe Rod (η = 5.98)

	vol fr (ex)	vol fr (th)	N (cm^{-1})	λ (ex) (μm)	λ (th) (μm)	t (ex) (μm)	t (th) (μm)	t (ruler) (μm)
AVERAGE ALL	**0.32**	**0.21**	**0.90**	**2.57**	**2.47**	**0.68**	**0.66**	
STDEV ALL	0.11	0.00	0.24	0.75	0.44	0.18	0.12	

Table C30. Minimum and Maximum Fe Fibers in Mg-12Li-2Nd/21Fe Rod (η = 5.98)

pic#	scope	mag	orient	min t (μm)	max t (μm)	max/min ratio
D289-	TEM	4400	T	0.11	5.68	50.00
D307-	TEM	3900	T	0.13	5.13	40.00
D315-	TEM	3900	T	0.13	5.64	44.00
0014	SEM	2000	T			
0015	SEM	5000	T			
0016	SEM	4940	T			
2419	SEM	3980	T			
0014	SEM	2000	T	0.15	5.25	35.00
0015	SEM	5000	T	0.10	1.40	14.00
AVERAGE ALL				**0.12**	**4.62**	**36.60**
STDEV ALL				0.02	1.82	13.78

Table C31. Stereological Measurements for the Mg-4Li/27Fe Casting ($\eta = 0$)

pic#	scope	mag	orient	vol fr (ex)	vol fr (th)	N (cm^{-1})	λ (ex) (μm)	λ (th) (μm)	t (ex) (μm)	t (th) (μm)	t (ruler) (μm)
2271	SEM	205	L		0.27	0.86	56.91	41.54		15.37	
2277	SEM	205	L		0.27	1.07	45.53	33.24		12.29	
2283	SEM	205	N		0.27	0.86	56.91	41.54		15.37	
2286	SEM	205	N		0.27	0.82	59.38	43.35		16.03	
2290	SEM	205	T		0.27	1.04	47.10	34.38		12.72	
2291	SEM	411	T		0.27	0.54	45.42	33.15		12.26	
2296	SEM	205	T		0.27	1.04	47.10	34.38		12.72	
2299	SEM	205	T		0.27	0.86	56.91	41.54		15.37	
2300	SEM	411	T		0.27	0.54	45.42	33.15		12.26	
2271	SEM	205	L	0.30	0.27	0.86	39.84	41.54	17.07	15.37	
2274	SEM	205	L	0.37	0.27	0.86	35.77	41.54	21.14	15.37	
2277	SEM	205	L	0.30	0.27	0.96	35.41	36.93	15.18	13.66	
2283	SEM	205	N	0.27	0.27	0.86	41.46	41.54	15.45	15.37	
2286	SEM	205	N	0.24	0.27	1.00	36.93	35.61	11.85	13.17	
2290	SEM	205	T	0.34	0.27	1.04	30.95	34.38	16.15	12.72	
2292	SEM	205	T	0.39	0.27	0.64	46.61	55.39	29.27	20.49	
2296	SEM	205	T	0.23	0.27	1.18	31.93	30.21	9.46	11.18	
2297	SEM	205	T	0.29	0.27	1.18	29.56	30.21	11.83	11.18	
2298	SEM	205	T	0.31	0.27	1.21	27.55	29.33	12.63	10.85	
2299	SEM	205	T	0.29	0.27	0.86	40.65	41.54	16.26	15.37	
2300	SEM	411	T	0.33	0.27	0.64	25.41	27.63	12.44	10.22	

Table C32. Average Stereological Measurements for the Mg-4Li/27Fe Casting ($\eta = 0$)

	vol fr (ex)	vol fr (th)	N (cm^{-1})	λ (ex) (μm)	λ (th) (μm)	t (ex) (μm)	t (th) (μm)	t (ruler) (μm)
AVERAGE ALL	**0.30**	**0.27**	**0.90**	**42.04**	**37.25**	**15.73**	**13.78**	
STDEV ALL	0.05	0.00	0.20	10.14	6.43	5.27	2.38	
AVERAGE ALL N	**0.26**	**0.27**	**0.88**	**48.67**	**40.51**	**13.65**	**14.98**	
STDEV ALL N	0.02	0.00	0.08	11.14	3.38	2.55	1.25	
AVERAGE ALL L	**0.32**	**0.27**	**0.92**	**42.69**	**38.96**	**17.80**	**14.41**	
STDEV ALL L	0.04	0.00	0.10	8.93	3.77	3.05	1.40	
AVERAGE ALL T	**0.31**	**0.27**	**0.90**	**39.55**	**35.44**	**15.43**	**13.11**	
STDEV ALL T	0.05	0.00	0.25	10.05	7.62	6.56	2.82	
AVERAGE ALL L + T	**0.31**	**0.27**	**0.90**	**40.47**	**36.48**	**16.14**	**13.49**	
STDEV ALL L + T	0.05	0.00	0.22	9.57	6.80	5.66	2.52	

Table C33. Minimum and Maximum Fe Fibers in the Mg-4Li/27Fe Casting ($\eta = 0$)

pic#	scope	mag	orient	min t (μm)	max t (μm)	max/min ratio
2271	SEM	205	L			
2277	SEM	205	L			
2283	SEM	205	N			
2286	SEM	205	N			
2290	SEM	205	T			
2291	SEM	411	T			
2296	SEM	205	T			
2299	SEM	205	T			
2300	SEM	411	T			
2271	SEM	205	L	7.32	24.39	3.33
2274	SEM	205	L	7.32	24.39	3.33
2277	SEM	205	L	7.32	29.27	4.00
2283	SEM	205	N	7.32	29.27	4.00
2286	SEM	205	N	4.88	24.39	5.00
2290	SEM	205	T	7.32	34.15	4.67
2292	SEM	205	T	14.63	39.02	2.67
2296	SEM	205	T	4.88	24.39	5.00
2297	SEM	205	T	4.88	24.39	5.00
2298	SEM	205	T	4.88	24.39	5.00
2299	SEM	205	T	7.32	26.83	3.67
2300	SEM	411	T	8.52	23.11	2.71
AVERAGE ALL				**7.21**	**27.33**	**4.03**
STDEV ALL				2.67	4.87	0.90
AVERAGE ALL N				**6.10**	**26.83**	**4.50**
STDEV ALL N				1.72	3.45	0.71
AVERAGE ALL L				**7.32**	**26.02**	**3.56**
STDEV ALL L				0.00	2.82	0.38
AVERAGE ALL T				**7.49**	**28.04**	**4.10**
STDEV ALL T				3.48	6.11	1.07
AVERAGE ALL L + T				**7.44**	**27.43**	**3.94**
STDEV ALL L + T				2.84	5.25	0.93

Table C34. Stereological Measurements for Mg-4Li/27Fe Rod (η = 2.69)

pic#	scope	mag	orient	vol fr (ex)	vol fr (th)	N (cm^{-1})	λ (ex) (μm)	λ (th) (μm)	t (ex) (μm)	t (th) (μm)	t (ruler) (μm)
2343	SEM	781	T		0.27	1.07	11.95	8.72		3.23	
2344	SEM	781	T		0.27	1.04	12.36	9.02		3.34	
2345	SEM	395	T		0.27	2.00	12.66	9.24		3.42	
2350	SEM	781	T		0.27	1.11	11.56	8.44		3.12	
2334	SEM	395	L	0.34	0.27	1.25	13.31	14.78	6.94	5.47	
2335	SEM	196	L		0.27						
2338	SEM	395	L	0.33	0.27	1.07	15.86	17.25	7.76	6.38	
2340	SEM	395	L	0.33	0.27	1.14	14.87	16.17	7.28	5.98	
2342	SEM	395	T	0.43	0.27	1.82	7.94	10.15	5.96	3.75	
2343	SEM	781	T	0.34	0.27	1.00	8.41	9.35	4.39	3.46	
2345	SEM	395	T	0.31	0.27	1.71	10.13	10.78	4.64	3.99	
2347	SEM	781	T	0.31	0.27	1.07	8.19	8.72	3.76	3.23	
2349	SEM	395	T	0.29	0.27	1.29	14.06	14.37	5.63	5.32	
2350	SEM	781	T	0.30	0.27	1.07	8.37	8.72	3.59	3.23	

Table C35. Average Stereological Measurements for Mg-4Li/27Fe Rod (η = 2.69)

	vol fr (ex)	vol fr (th)	N (cm^{-1})	λ (ex) (μm)	λ (th) (μm)	t (ex) (μm)	t (th) (μm)	t (ruler) (μm)
AVERAGE ALL	**0.33**	**0.27**	**1.28**	**11.51**	**11.21**	**5.55**	**4.15**	
STDEV ALL	0.04	0.00	0.34	2.70	3.21	1.55	1.19	
AVERAGE ALL T	**0.33**	**0.27**	**1.32**	**10.56**	**9.75**	**4.66**	**3.61**	
STDEV ALL T	0.05	0.00	0.38	2.23	1.78	0.97	0.66	

Table C36. Minimum and Maximum Fe Fibers in Mg-4Li/27Fe Rod (η = 2.69)

pic#	scope	mag	orient	min t (μm)	max t (μm)	max/min ratio
2343	SEM	781	T			
2344	SEM	781	T			
2345	SEM	395	T			
2350	SEM	781	T			
2334	SEM	395	L	1.27	18.99	15.00
2335	SEM	196	L	5.10	56.12	11.00
2338	SEM	395	L	2.53	20.25	8.00
2340	SEM	395	L	2.53	16.46	6.50
2342	SEM	395	T	1.90	15.19	8.00
2343	SEM	781	T	1.92	14.08	7.33
2345	SEM	395	T	1.27	17.72	14.00
2347	SEM	781	T	1.28	14.08	11.00
2349	SEM	395	T	1.27	12.66	10.00
2350	SEM	781	T	1.92	9.60	5.00
AVERAGE ALL				**2.10**	**19.52**	**9.58**
STDEV ALL				1.17	13.23	3.23
AVERAGE ALL T				**1.59**	**13.89**	**9.22**
STDEV ALL T				0.35	2.70	3.15

Table C37. Stereological Measurements for Mg-4Li/27Fe Rod (η = 3.92)

pic#	scope	mag	orient	vol fr (ex)	vol fr (th)	N (cm^{-1})	λ (ex) (μm)	λ (th) (μm)	t (ex) (μm)	t (th) (μm)	t (ruler) (μm)
0133	SEM	1000	T	0.28	0.27	0.85	8.44	8.60	3.35	3.18	
0134	SEM	500	T	0.30	0.27	1.55	9.12	9.45	3.82	3.49	
0135	SEM	500	T	0.28	0.27	1.67	8.59	8.76	3.41	3.24	
0136	SEM	1000	T	0.31	0.27	1.09	6.35	6.69	2.81	2.48	
0137	SEM	1000	T	0.39	0.27	1.15	5.33	6.34	3.36	2.34	
0138	SEM	500	T	0.25	0.27	1.61	9.34	9.09	3.11	3.36	

Table C38. Average Stereological Measurements for Mg-4Li/27Fe Rod (η = 3.92)

	vol fr (ex)	vol fr (th)	N (cm^{-1})	λ (ex) (μm)	λ (th) (μm)	t (ex) (μm)	t (th) (μm)	t (ruler) (μm)
AVERAGE ALL	**0.30**	**0.27**	**1.32**	**7.86**	**8.16**	**3.31**	**3.02**	
STDEV ALL	0.05	0.00	0.33	1.63	1.31	0.34	0.48	

Table C39. Minimum and Maximum Fe Fibers in Mg-4Li/27Fe Rod (η = 3.92)

pic#	scope	mag	orient	min t (μm)	max t (μm)	max/min ratio
0133	SEM	1000	T	0.50	12.00	24.00
0134	SEM	500	T	0.60	23.00	38.33
0135	SEM	500	T	0.40	17.00	42.50
0136	SEM	1000	T	0.30	16.50	55.00
0137	SEM	1000	T	0.50	10.00	20.00
0138	SEM	500	T	0.80	16.00	20.00
AVERAGE ALL				**0.52**	**15.75**	**33.31**
STDEV ALL				0.17	4.51	14.29

APPENDIX D. EXTRANEOUS MICROGRAPHS

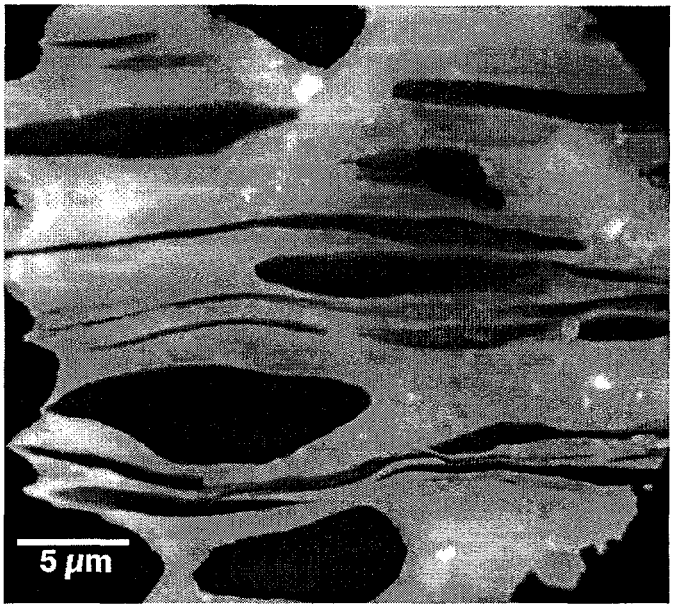

Figure 1. Dark-field TEM micrograph of BCC/BCC Mg-12Li-2Nd/21Fe sheet rolled to $\eta = 3.67$ at room temperature (transverse section).

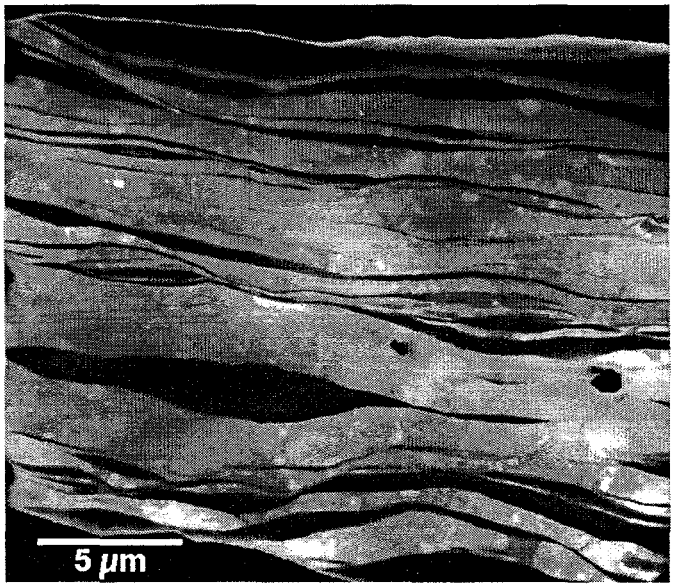

Figure 2. Dark-field TEM micrograph of BCC/BCC Mg-12Li-2Nd/21Fe sheet rolled to $\eta = 6.5$ at room temperature (transverse section).

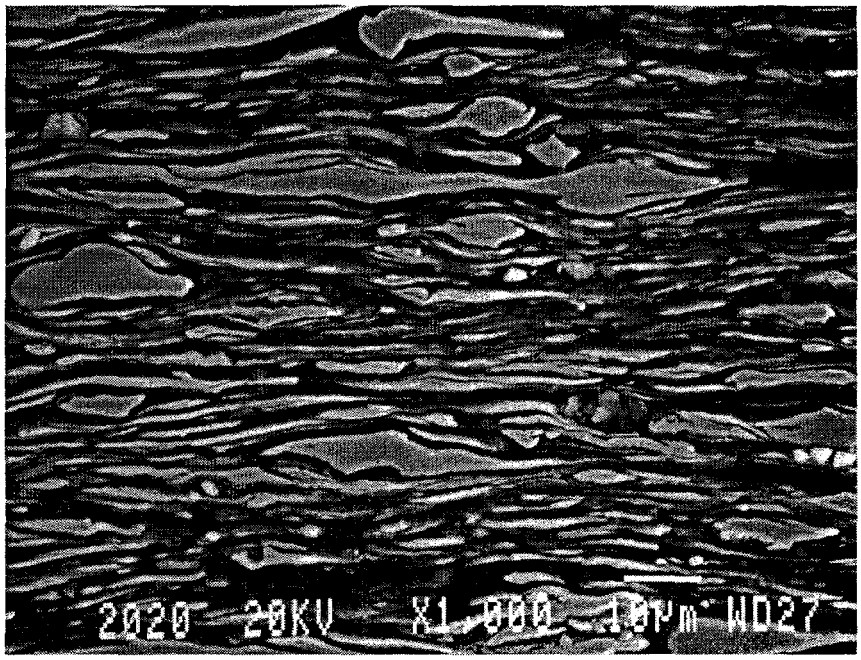

(a)

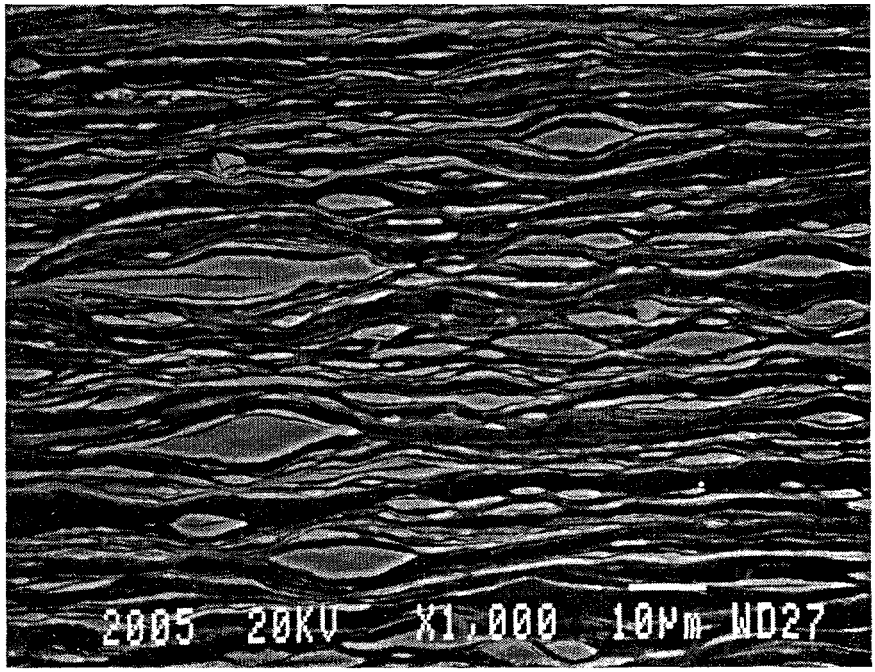

(b)

Figure 3. SEM micrographs of (a) transverse and (b) longitudinal sections of BCC/BCC Mg-12Li-2Nd/21Fe sheet rolled to $\eta = 6.5$ at room temperature.

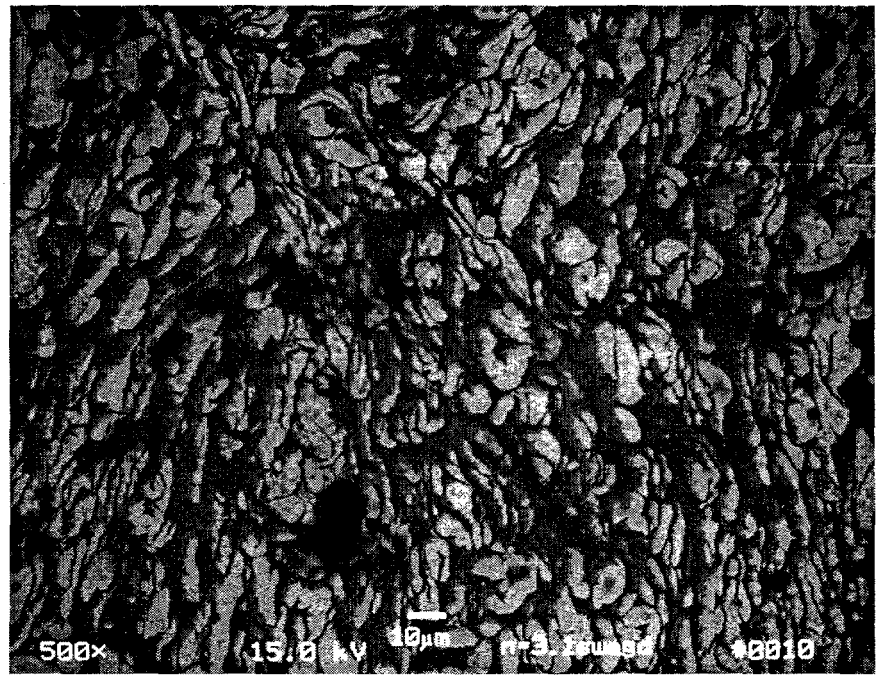

Figure 4. BCC/BCC Mg-12Li-2Nd/21Fe rod swaged to η = 3.1 at room temperature (transverse section) showing the internal cracking observed in much of the rod material at this level of deformation.

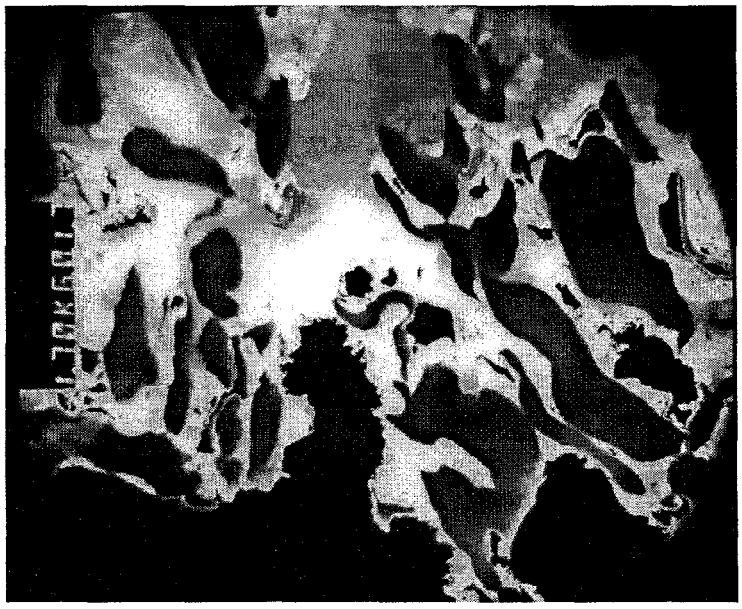

Figure 5. Dark-field TEM of BCC/BCC Mg-12Li-2Nd/21Fe rod swaged to η = 3.1 at room temperature (transverse section).

Figure 6. TEM montage of Mg-12Li-2Nd/21Fe rod swaged to $\eta = 4.3$ (transverse section).

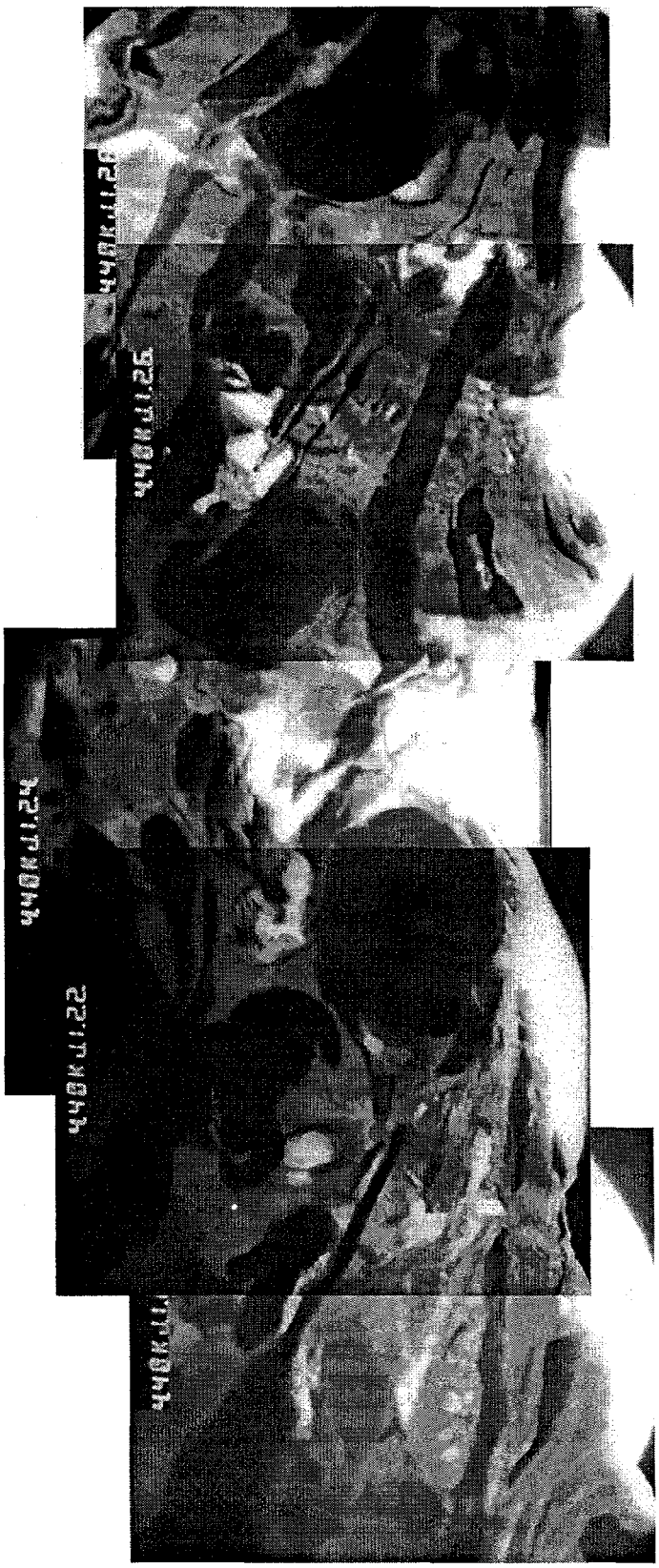

Figure 7. TEM montage of Mg-12Li-2Nd/21Fe rod swaged to $\eta = 4.3$ (transverse section).

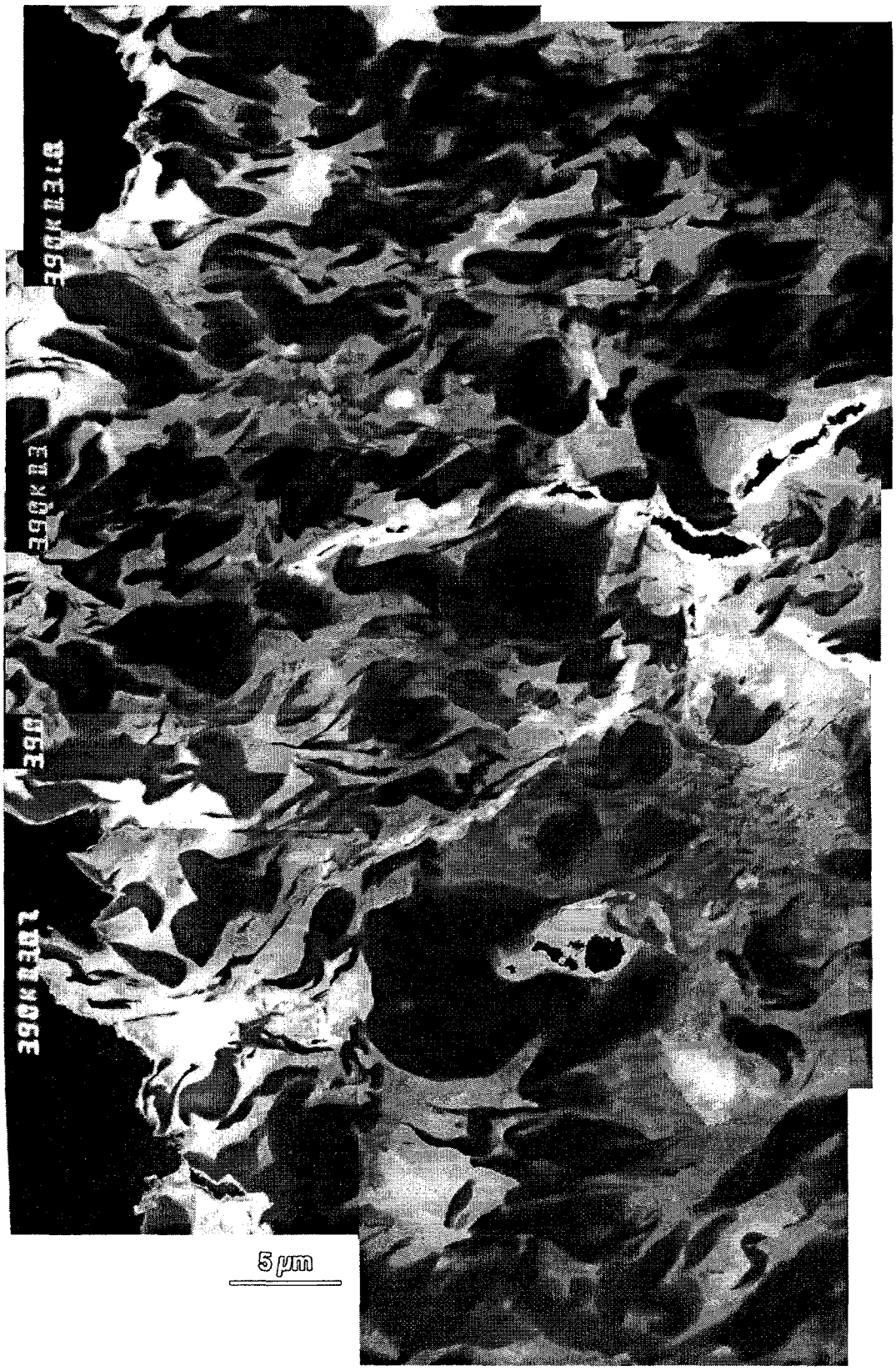

Figure 8. TEM montage of Mg-12Li-2Nd/21Fe rod swaged to $\eta = 6.0$ (transverse section).

Figure 9. TEM montage of Mg-12Li-2Nd/21Fe rod swaged to $\eta = 6.0$ (transverse section).

Figure 10. Mg-12Li-2Nd/21Fe rod swaged to $\eta = 6.0$ (transverse section).

Figure 11. Mg-12Li-2Nd/21Fe rod swaged to $\eta = 6.0$ (transverse section).

APPENDIX E: MECHANICAL PROPERTIES

Best-fit polynomial equations were used to fit the experimental tensile data for the matrix alloys (Mg-4Li and Mg-12Li-2Nd) and AISI 1011 steel deformed individually as rod and sheet products. The polynomial equations in Table I were used in the calculation of rule of mixtures (ROM) strength predictions presented in this dissertation. The original ultimate tensile strength (UTS) data are also included and reported in MPa. Italicized data in the tables were deemed to be invalid measurements.

Table I. Matrix and Fiber Material Strength Related to Deformation

Material	Product	Polynomial Fit	Correlation Coefficient (R)
1011 Steel	Rod	$\sigma = 480 + 195.51\eta + 16.986\eta^2$	0.97945
	Sheet	$\sigma = 480 + 206.03\eta_e - 14.183\eta_e^2$	0.98766
Mg-4Li	Rod	$\sigma = 125 + 10.195\eta + 3.8924\eta^2$	0.99661
	Sheet	$\sigma = 125 + 10.896\eta_e - 0.43491\eta_e^2$	0.99047
Mg-12Li-2Nd	Rod	$\sigma = 106 + 5.7351\eta + 0.54004\eta^2$	0.96125
	Sheet	$\sigma = 106 + 13.074\eta_e - 1.0554\eta_e^2$	0.97188

σ = ultimate tensile strength (MPa)
η = true deformation strain
η_e = effective deformation strain (for sheet)

Table II. Tensile Strength of AISI 1011 Steel

Strain (η_e)	Sheet UTS	Strain (η)	Rod UTS
0.00	434.1	0.00	497.8
0.00	434.1	0.00	529.8
0.00	428.0	0.00	520.6
2.10	837.1	0.00	520.5
2.10	882.1	0.57	698.6
2.10	863.5	0.57	731.9
3.40	1003.6	0.57	722.1
3.40	996.6	1.40	849.4
3.40	1033.8	1.40	1101.4
4.40	1123.7	1.40	1106.7
4.40	1137.1	1.40	848.8
4.40	1049.8	2.80	1093.6
4.40	1101.0	2.80	1101.8
5.10	1224.7	2.80	1079.6
5.10	1123.7	2.80	1099.7
5.20	1103.0	4.20	1371.6
5.20	1236.3	4.20	1367.4
		4.20	1566.0
		4.20	1523.0
		5.50	2188.1
		5.50	2125.6
		5.50	2126.8
		5.50	2127.2
		6.20	2394.5
		6.20	2279.7
		6.20	2408.5

Table III. Tensile Strength of Mg-4Li Matrix

Strain (η_e)	Sheet UTS	Strain (η)	Rod UTS
0.00	124.1	0.00	124.1
0.00	123.4	0.00	123.4
0.00	125.1	0.00	125.1
0.00	127.8	0.00	127.8
2.07	147.5	1.72	159.7
2.07	148.5	1.72	158.6
2.07	150.0	2.73	176.8
2.07	145.3	2.73	176.4
3.96	158.5	4.33	241.6
3.96	156.7	4.33	245.2
3.96	160.6		
6.59	180.0		
6.59	181.0		
6.59	174.2		

Table IV. Tensile Strength of Mg-4Li/27Fe

Strain (η)	Rod UTS
0.00	166.1
0.00	154.7
0.00	172.9
0.00	157.5
2.70	285.8
2.70	286.7
3.92	335.9
3.92	330.8
3.92	329.9
4.99	*307.3*

Table V. Tensile Strength of Mg-12Li-2Nd Matrix

Strain (η_e)	Sheet UTS	Strain (η)	Rod UTS
0.00	102.7	0.00	102.7
0.00	102.7	0.00	102.7
0.00	106.8	0.00	106.8
0.00	111.7	0.00	111.7
2.07	132.1	1.72	119.1
2.07	134.9	1.72	117.0
2.07	132.7	1.72	118.3
4.14	135.1	2.93	135.4
4.14	139.4	2.93	133.3
4.14	138.8	4.37	130.4
6.21	147.3	4.37	131.1
6.21	145.1	5.75	161.1
6.21	146.8	5.75	158.3
6.21	149.7	5.75	159.6
6.21	145.1		
6.98	149.5		
6.98	147.5		
6.98	150.2		
6.98	142.0		
6.98	142.0		

Table VI. Tensile Strength of Mg-12Li-2Nd/21Fe Composite

Strain (η_e)	Sheet UTS	Strain (η)	Rod UTS
0.00	182.9	0.00	182.9
0.00	176.2	0.00	176.2
1.89	206.1	3.07	228.7
1.89	215.3	3.07	230.8
1.89	213.3	4.29	329.0
1.89	210.8	4.29	322.5
4.00	243.0	*5.98*	*317.9*
4.00	247.1	*5.98*	*326.5*
4.00	245.5	*5.98*	*304.7*
4.00	241.5	*5.98*	*328.5*
5.55	267.6	*5.98*	*321.4*
5.55	250.0	*5.98*	*301.4*
5.55	257.7	*7.01*	*198.4*
5.55	248.5	*7.01*	*211.4*
6.47	*266.8*		
6.47	*283.3*		
6.47	*273.5*		
6.47	*278.2*		
6.47	*279.6*		
6.47	*267.3*		
6.47	*277.3*		
6.47	*283.9*		
6.47	*278.0*		
6.47	*275.9*		
6.47	*272.7*		
6.54	315.9		
6.54	308.8		
6.54	298.3		
8.60	262.5		
8.60	339.0		
8.60	322.1		